

Figure 2.1: ZnO crystal structures. Redrawn from ref [1].

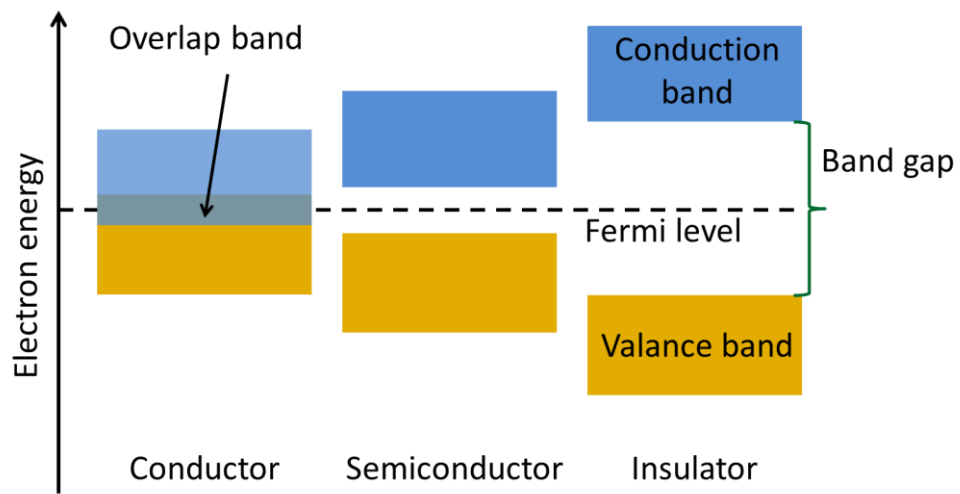


Figure 2.2: Band gap energy diagram of the conductor, semiconductor and an insulator. Redrawn from ref [2].

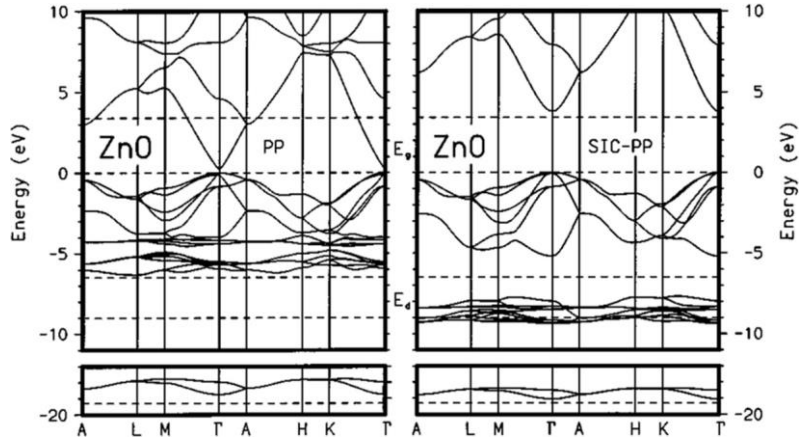


Figure 2.3: LDA bulk band structure of ZnO as calculated using standard pseudopotentials (PP) method on the left panel and self-interaction-corrected pseudopotentials (SIC-PP) method on the right panel. All energies are measured with respect to the top of the valence band. The horizontal dashed lines indicate the measured gap energy [3].

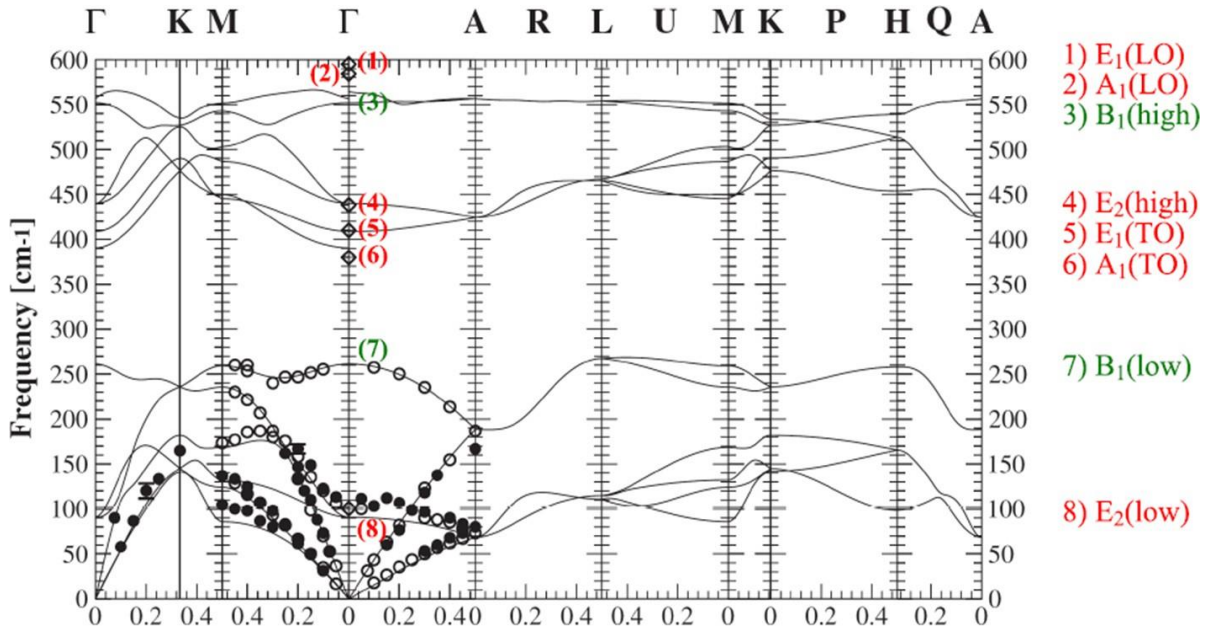


Figure 2.4: Phonon dispersion relationship of wurtzite zinc oxide is calculated at  $\Gamma$  point in the specified direction of the Brillouin zone center by using the lattice dynamics equation. Molecular vibration represented by red font ( $E_1$ ,  $E_2$ ,  $A_1$ ) can be observed through Raman scattering, while  $B_1$  mode represented by green font can't be observed through Raman scattering. [4].

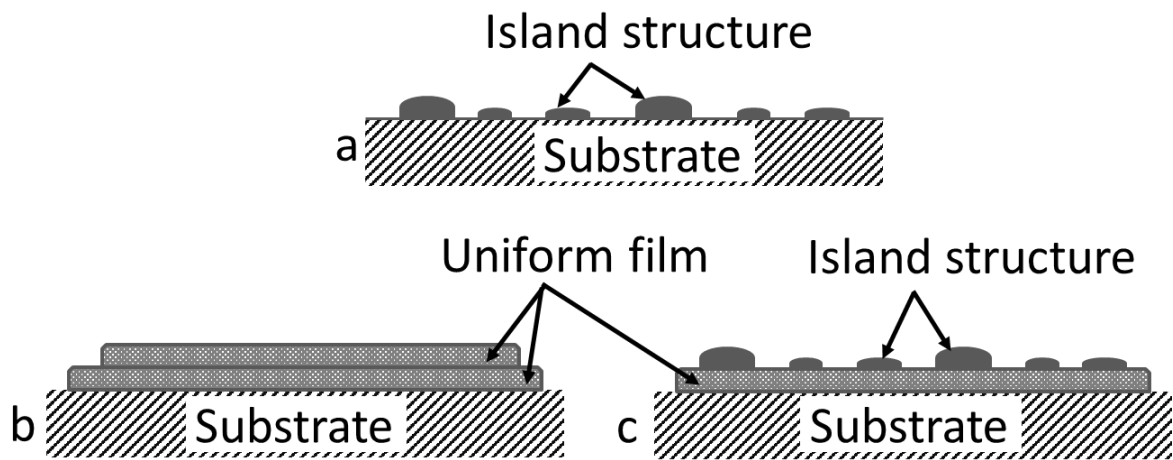


Figure 2.5: The modes of thin films growth processes (a) Volmer-Weber type (b) Frank-van der Merwe type (c) Stranski-Krastanov type. Redrawn from ref [5].

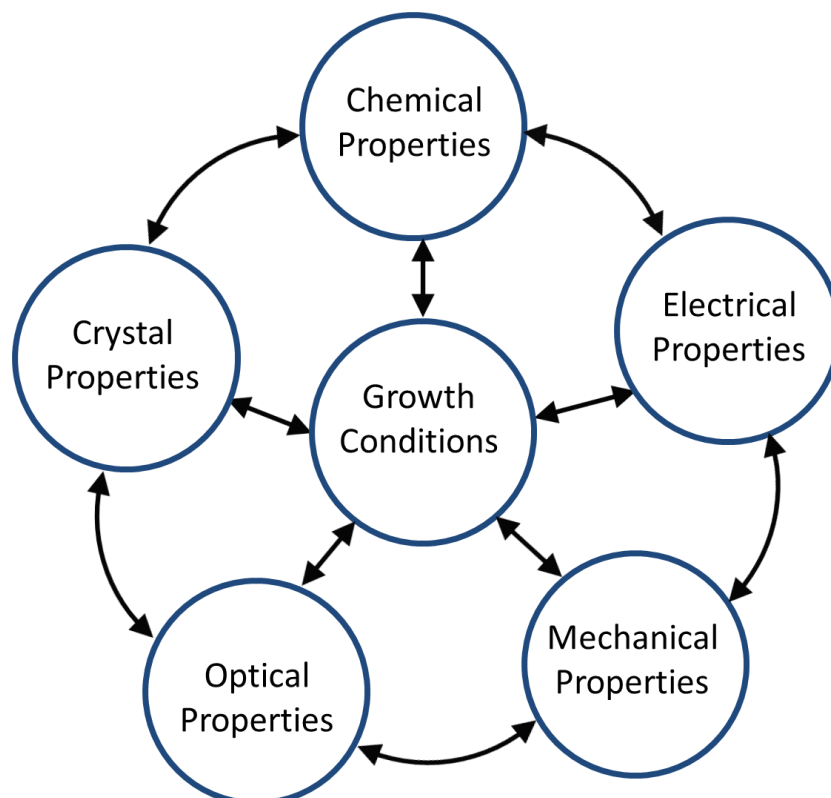


Figure 2.6: Correlations between growth conditions and the properties of the resultant thin films. Redrawn from ref [5].

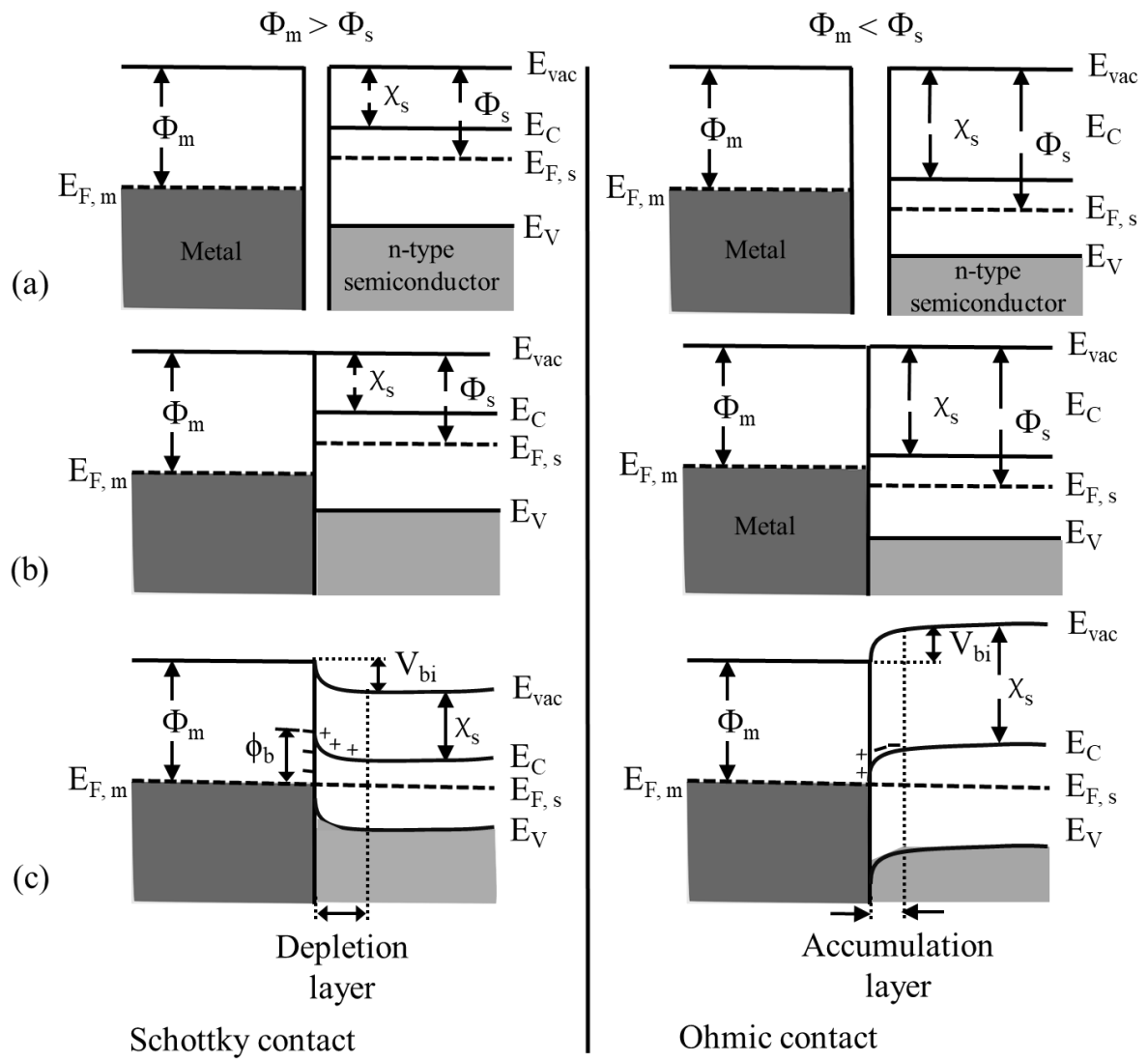


Figure 2.7: Energy band diagrams of metal and n-type semiconductor contacts (a) not in contact (b) in contact (c) in contact under equilibrium. Redrawn from ref [6].

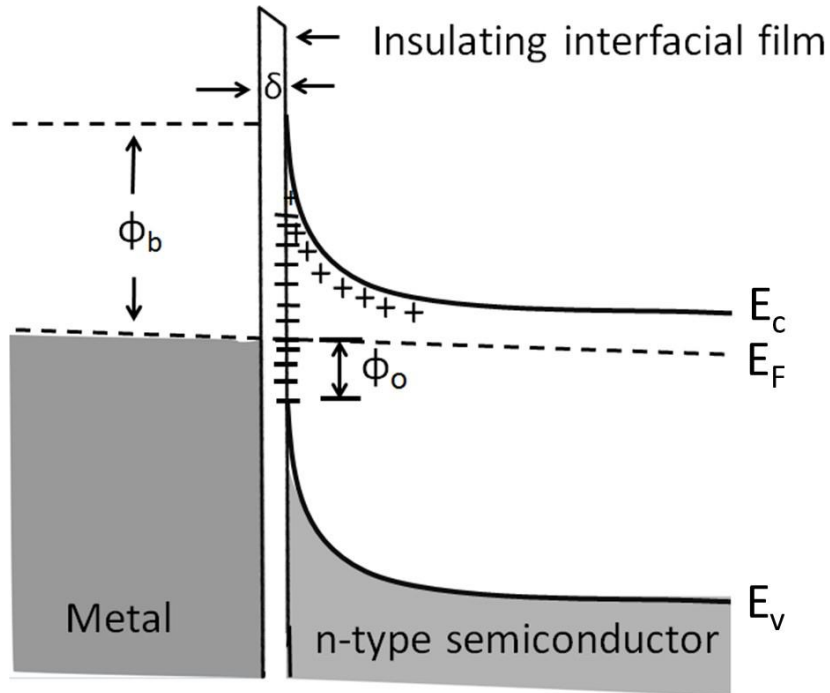


Figure 2.8: Electron energy band diagram of a metal-semiconductor contact with surface states and interfacial layer. Redrawn from ref [7].

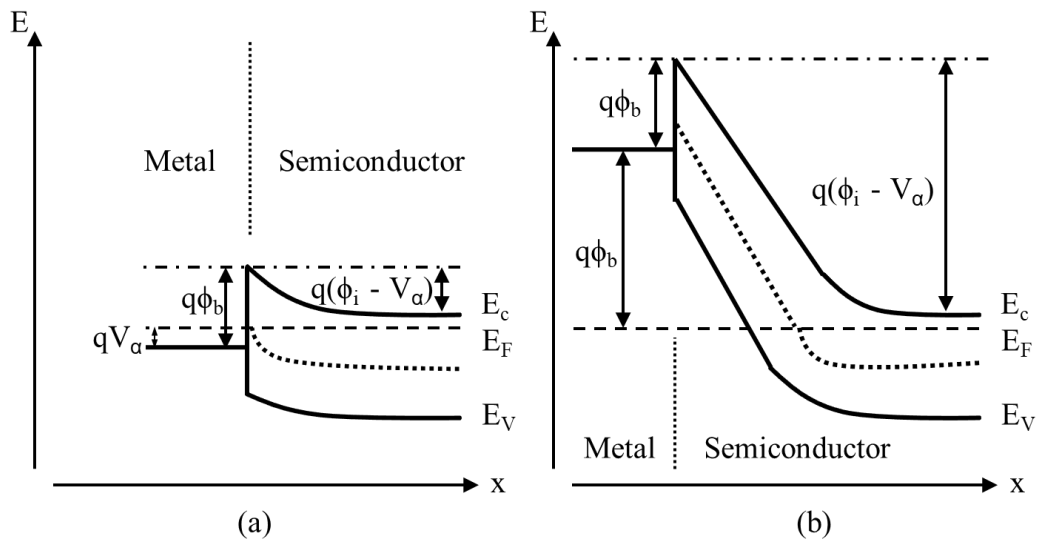


Figure 2.9: Electron energy band diagram of a metal-semiconductor contact under (a) forward bias (b) reverse bias. Redrawn from ref [2].

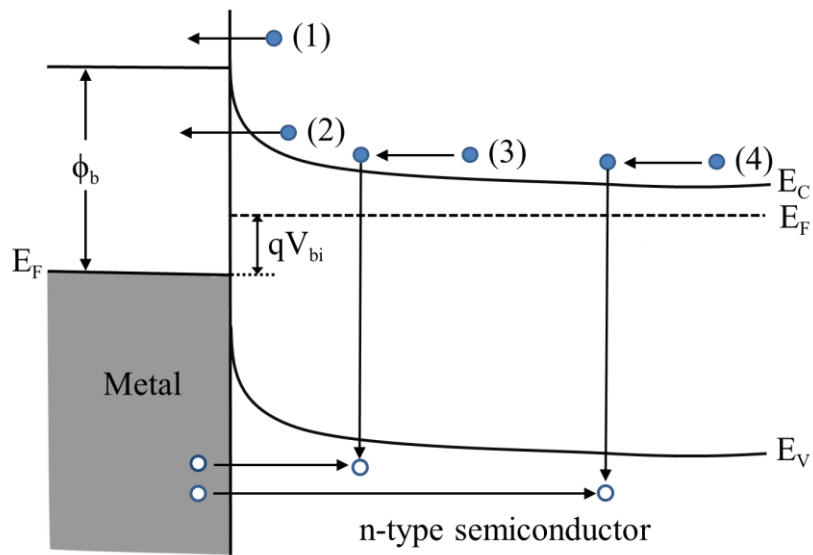


Figure 2.10: The basic transport processes in forward biased Schottky barrier on an n-type semiconductor. These are (1) thermionic emission, (2) Quantum-mechanical tunneling, (3) carrier generation and recombination and (4) hole injection. Redrawn from ref [8].

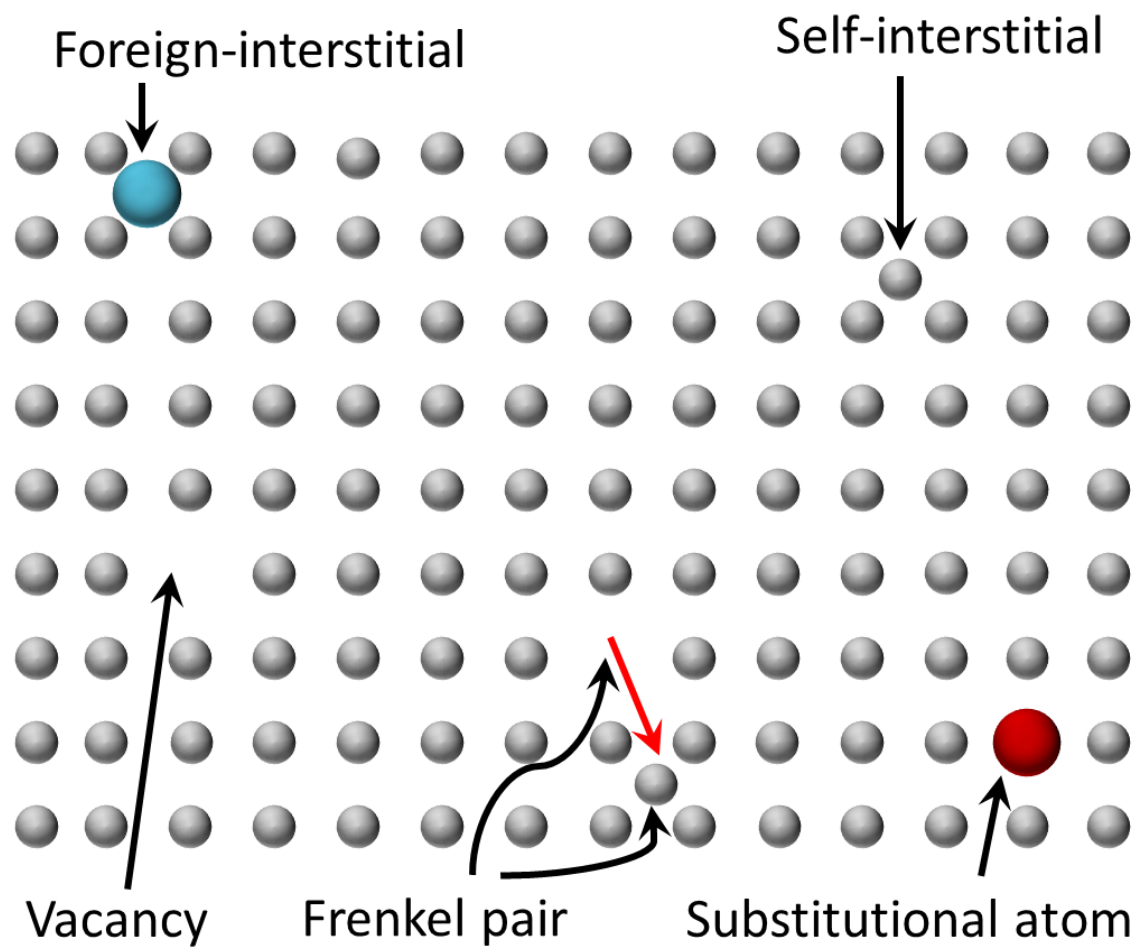


Figure 2.11: A schematic diagram of point defects. Redrawn from ref [9].



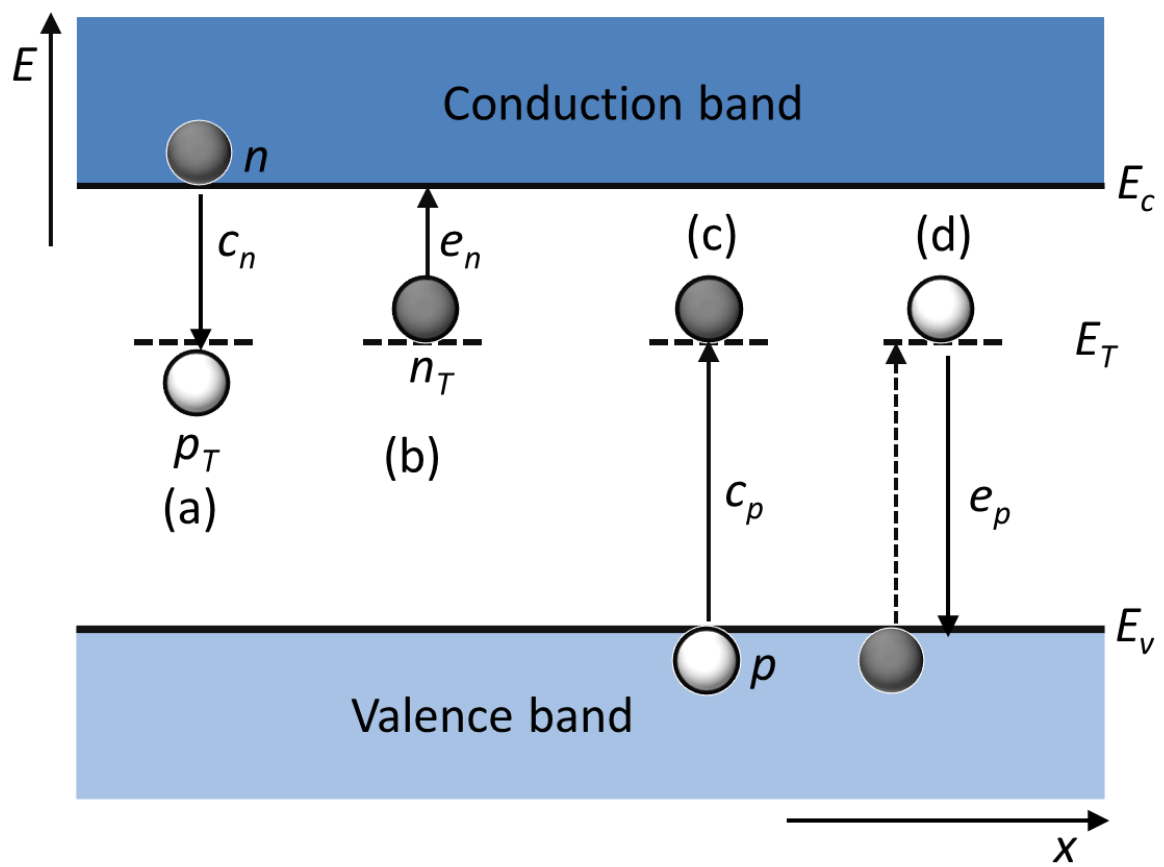


Figure 2.12: Electron energy band diagram for a semiconductor with deep-level impurities. Redrawn from ref [10].

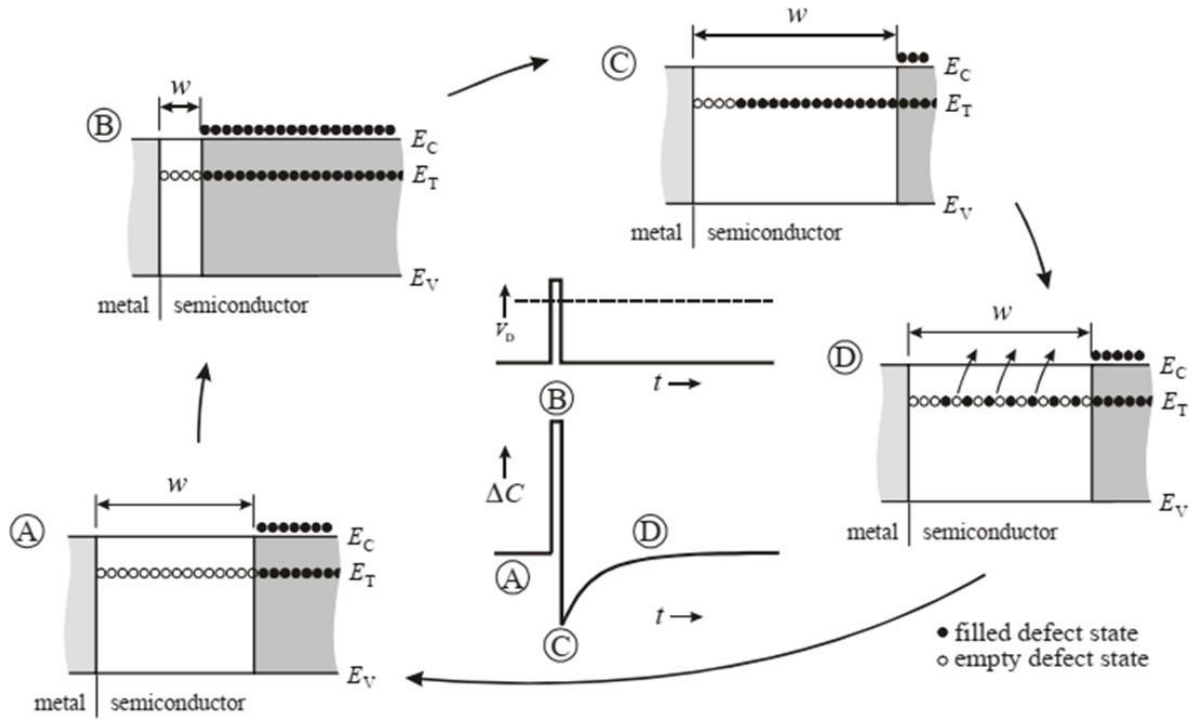


Figure 2.13: Variation of depletion region width and trap population of an electron trap in n-type semiconductor for a DLTS bias and filling pulse cycle. (A) and (B) are during reverse bias and the filling pulse, respectively, whereas (C) is directly after removing the filling pulse and (D) at a time  $t$  after (C). The resultant capacitance transient is qualitatively shown in the center of the figure [11].

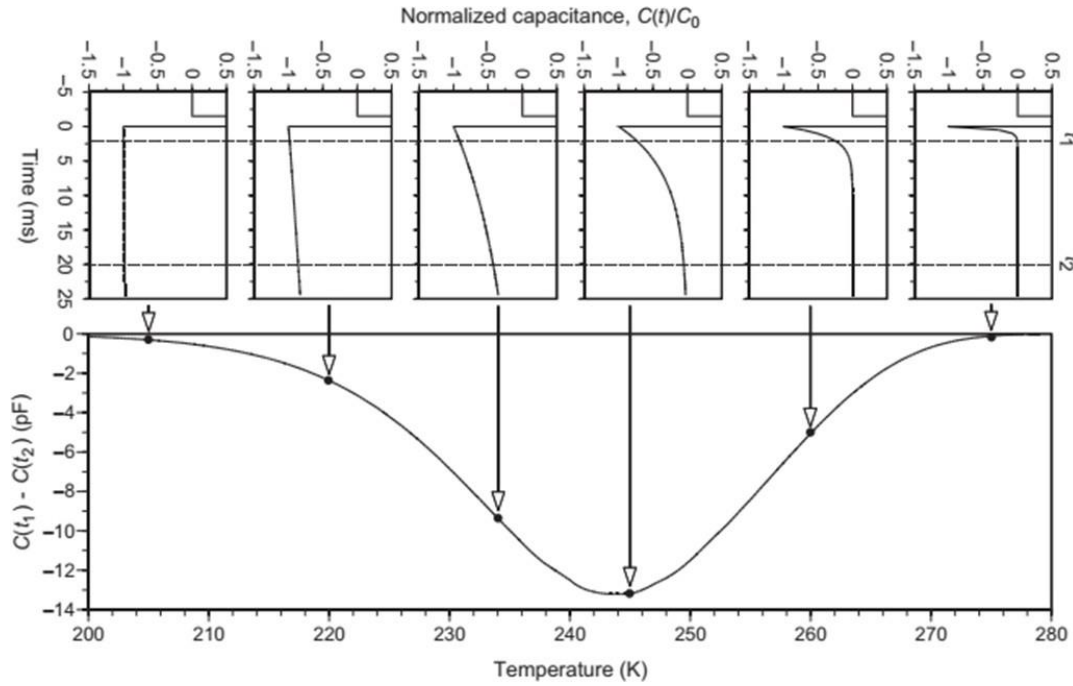


Figure 2.14: Temperature dependence of time constant of capacitance transient (top), and the DLTS signal obtained from the transient as a function of sample temperature (bottom) [12].

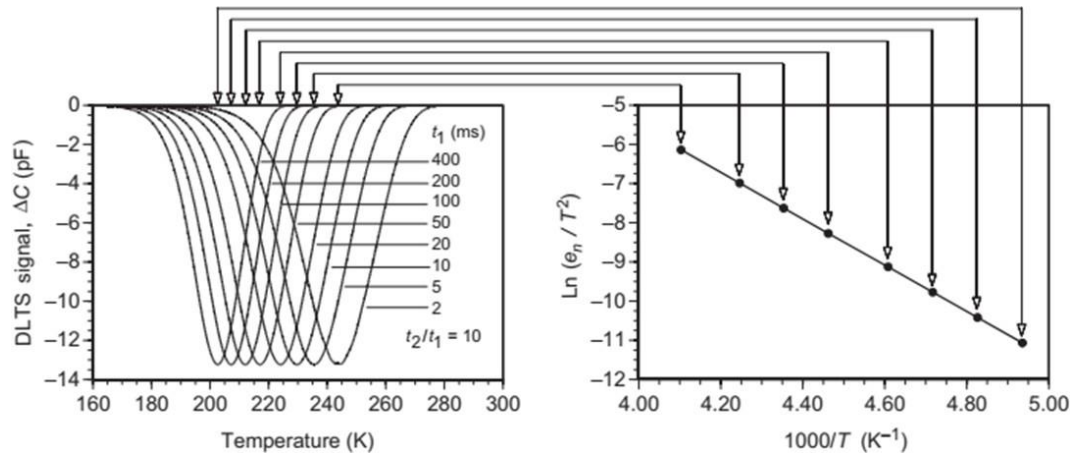


Figure 2.15: Deriving an Arrhenius plot from DLTS signals. The DLTS signals are measured at different values of  $t_1$  with  $t_2/t_1 = 10$  [12].

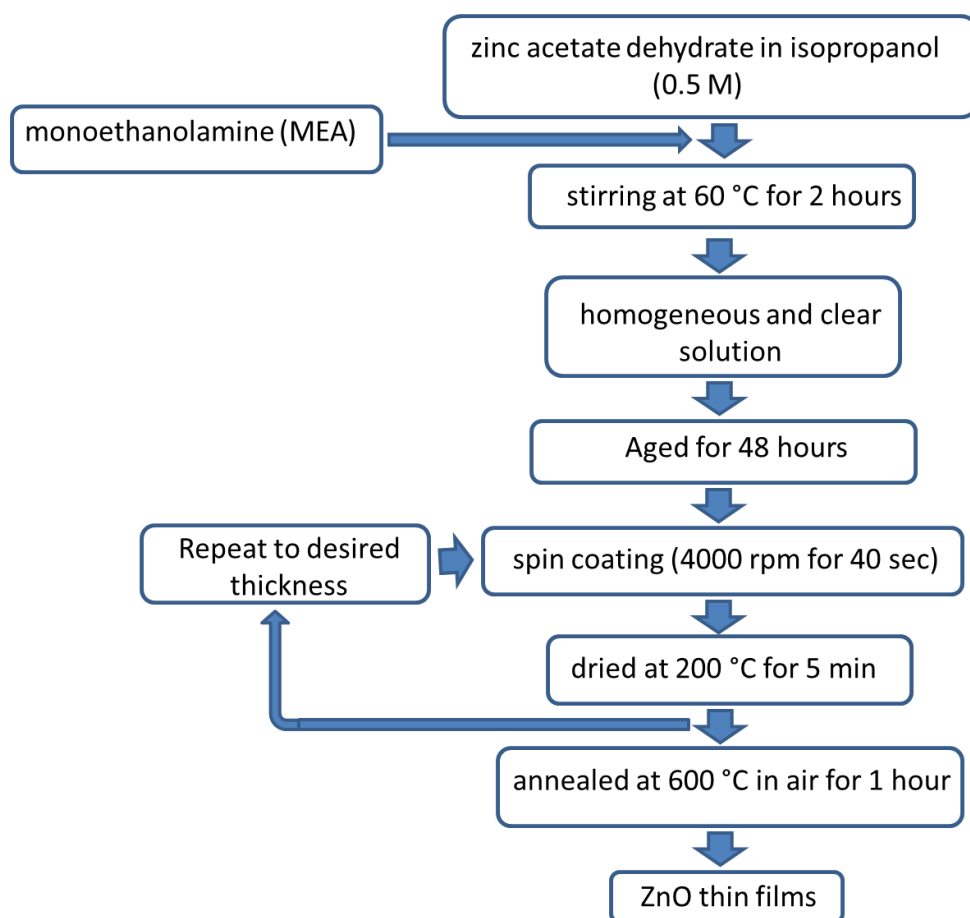


Figure 3.1: A schematic diagram of the preparation of ZnO thin films using the sol-gel spin coating method.

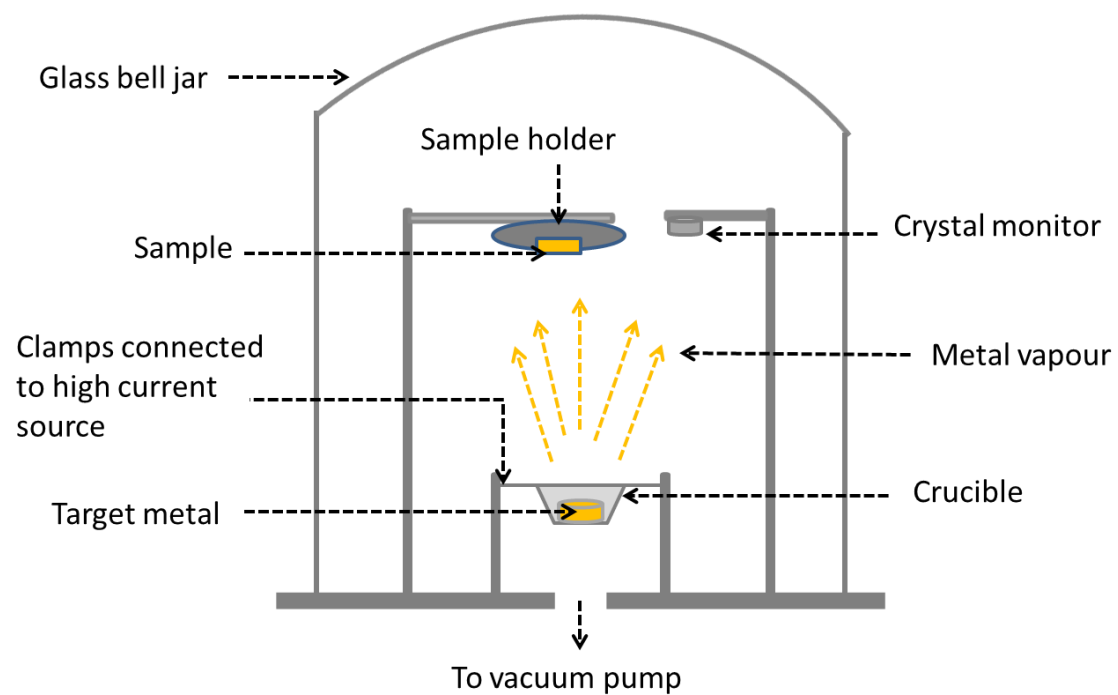


Figure 3.2: A schematic diagram of the resistive evaporation technique.

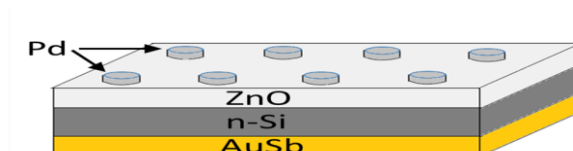


Figure 3.3: Schematic representation of the devices used for electrical measurements consisting of the Au-Sb ohmic contact, Si substrate, the ZnO thin film, and the Pd Schottky contacts.

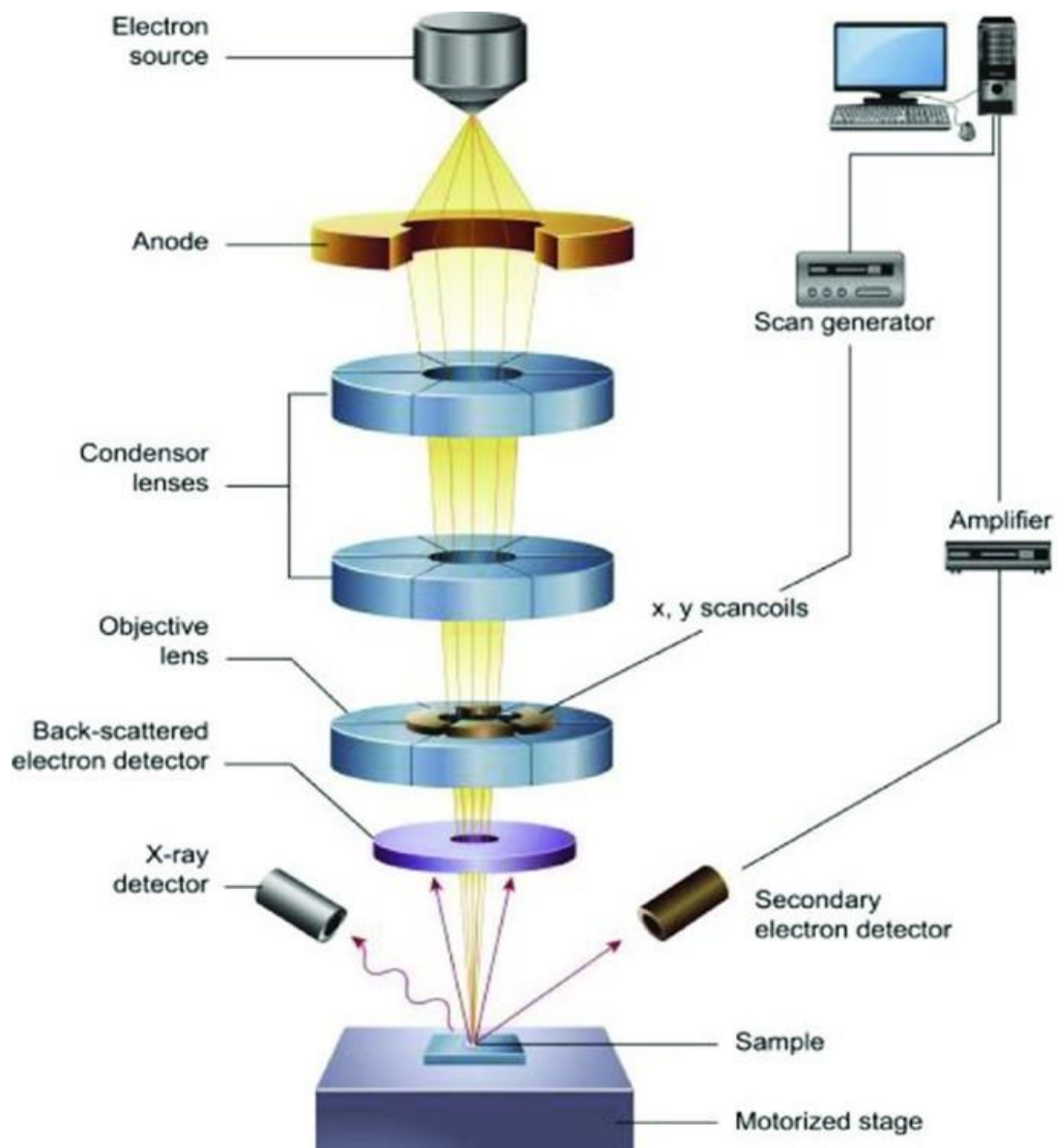


Figure 3.4: Scanning electron microscopy system [13].

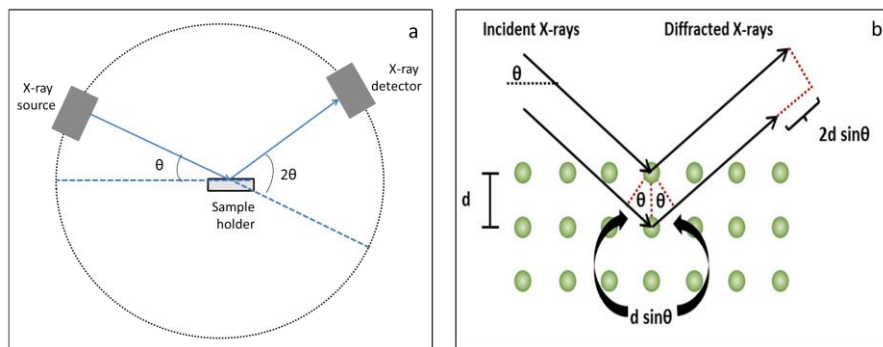


Figure 3.5: A schematic diagram of (a) a typical arrangement of XRD diffractometer components (b) Bragg analysis for X-ray diffraction by crystal planes [14].

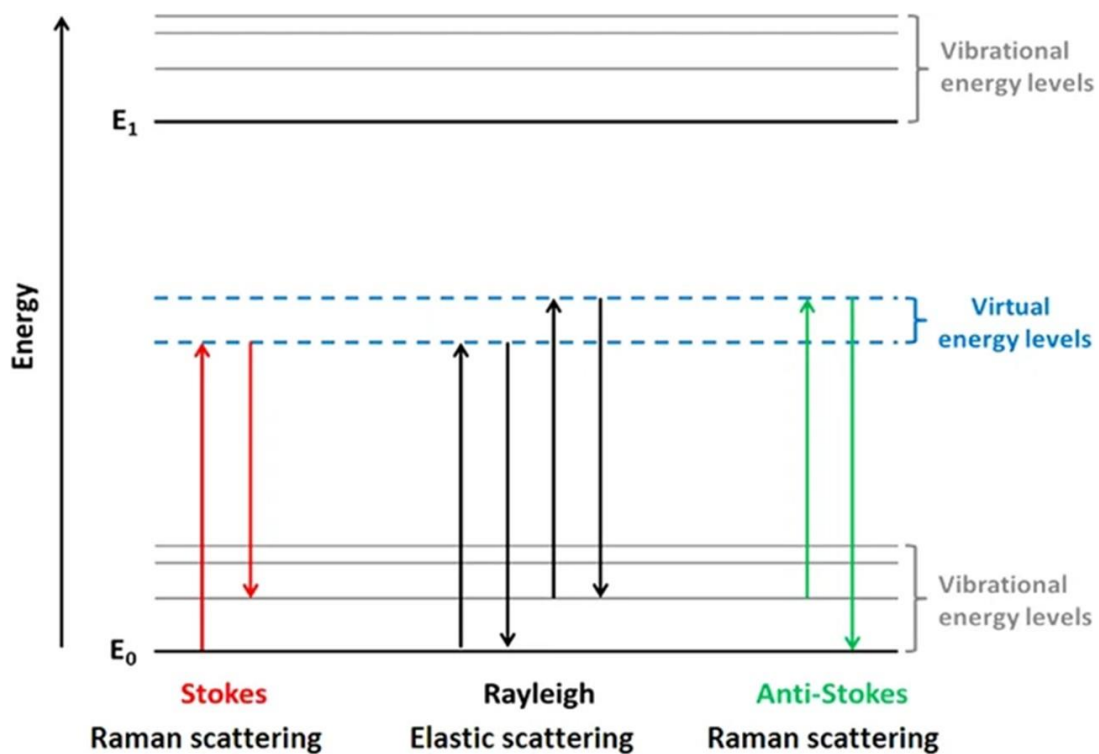


Figure 3.6: Jablonski style diagram of energetic transitions involved in Raman scattering [15].

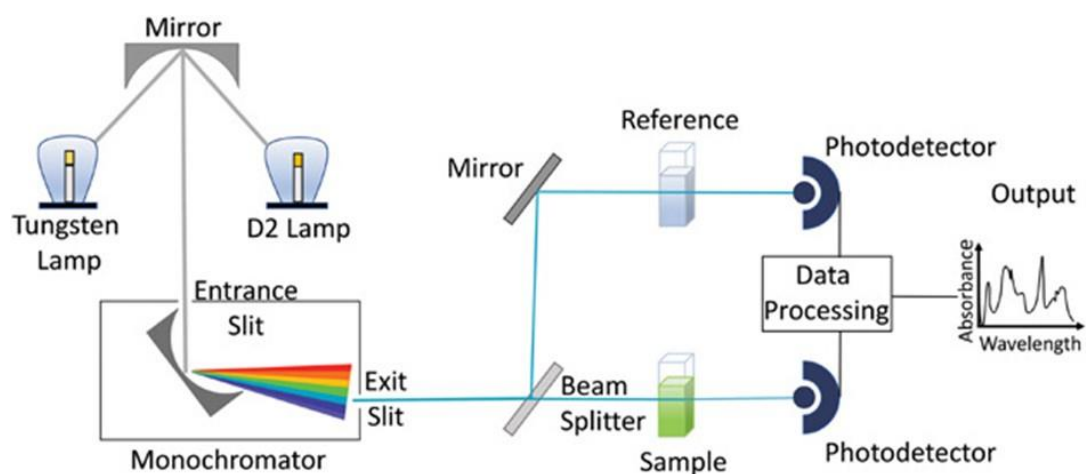


Figure 3.7: A Schematic diagram of a dual-beam UV-Vis spectrometer [16].

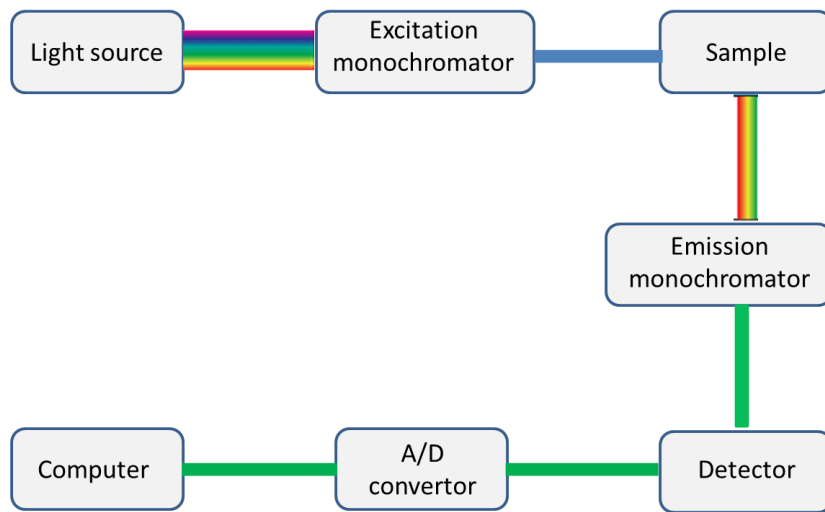


Figure 3.8: A schematic diagram of photoluminescence spectroscopy.

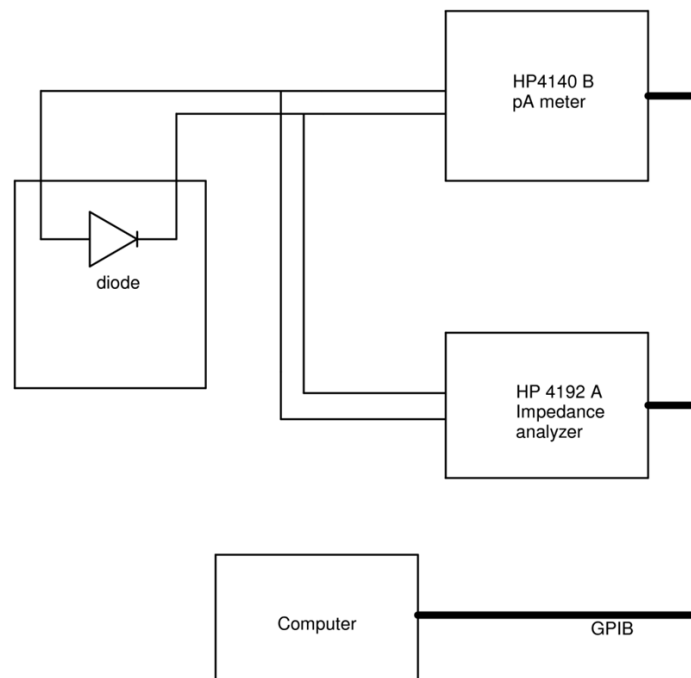


Figure 3.9: A block diagram of  $I$ - $V$  and  $C$ - $V$  measurements system [17].



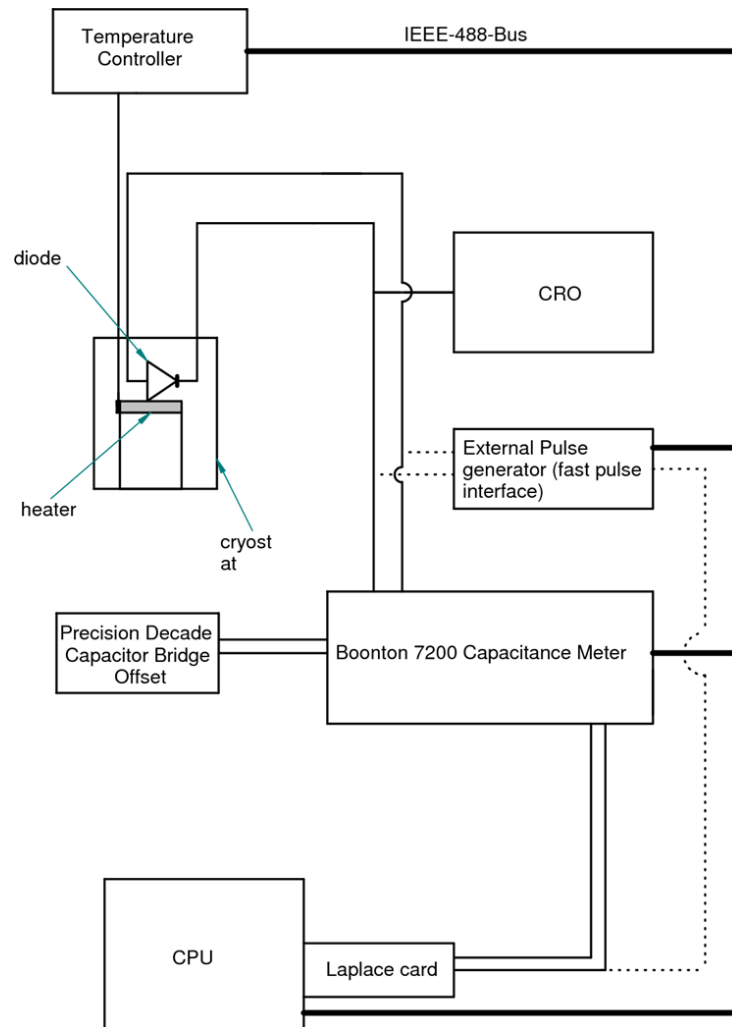


Figure 3.10: Schematic diagram of the DLTS and Laplace DLTS system. The dotted lines show the necessary connections when an external pulse generator is used [17].

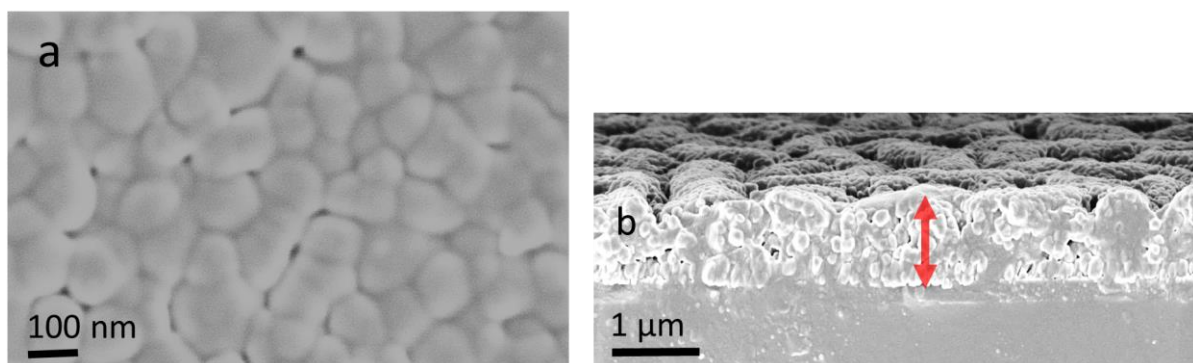


Figure 4.1: SEM images of the (a) surface and (b) cross-section of ZnO thin films deposited on ITO/glass substrate.

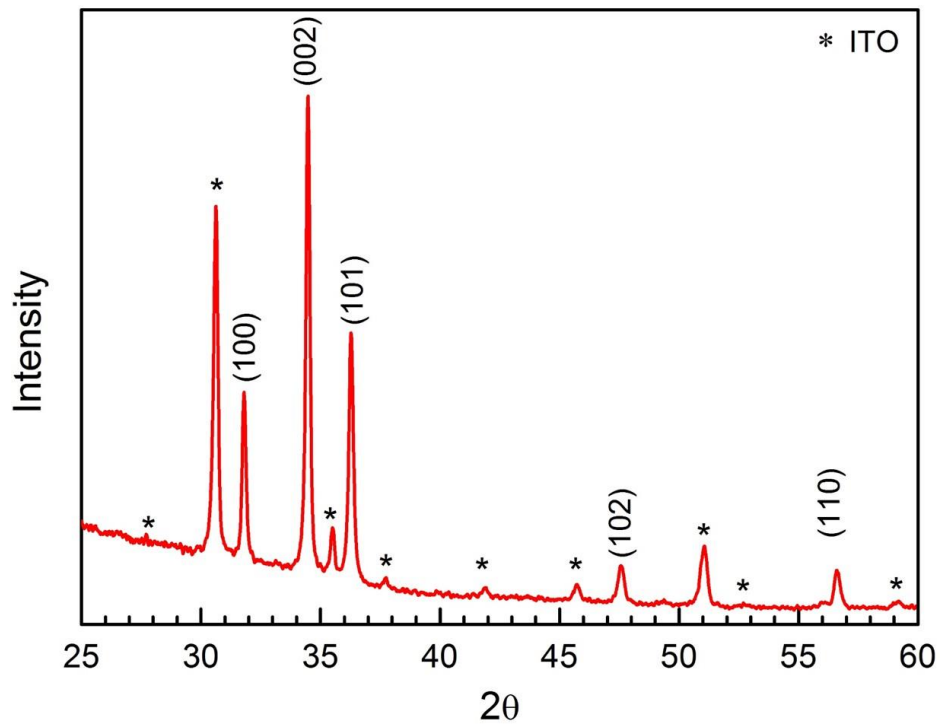


Figure 4.2: The X-ray diffraction (XRD) patterns of ZnO thin films deposited onto ITO/glass substrate after annealing at 600 °C.

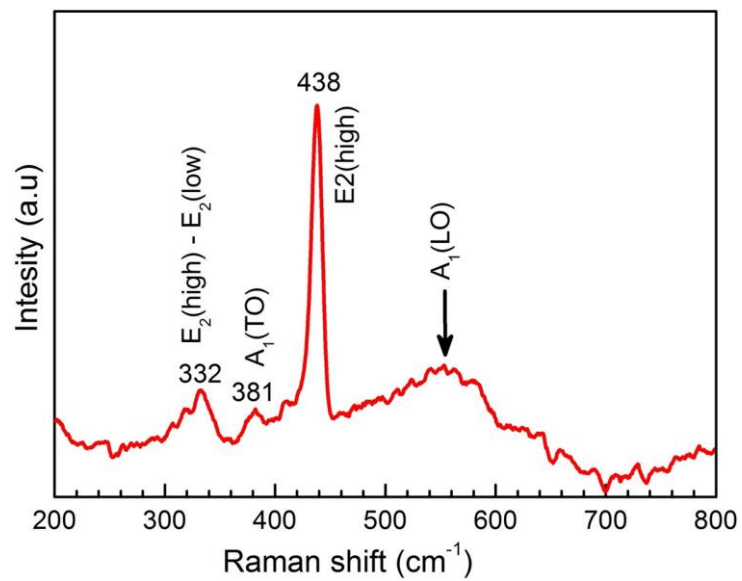


Figure 4.3: The Raman spectra of a ZnO thin film deposited onto ITO/glass substrate after annealing at 600 °C.

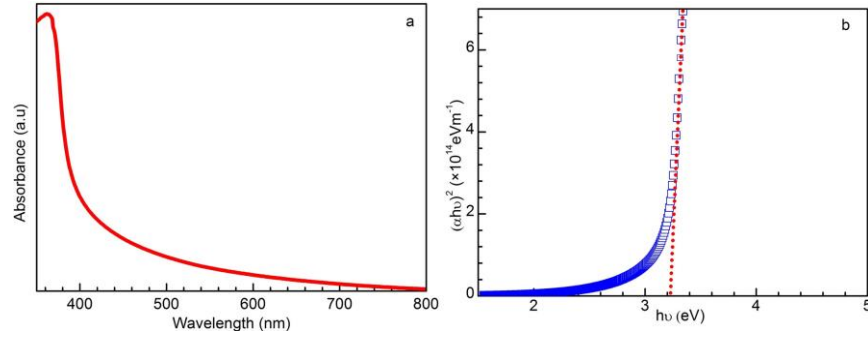


Figure 4.4: UV-Vis spectra of ZnO thin films deposited on ITO substrate (a) Absorbance (b) Tauc plot.

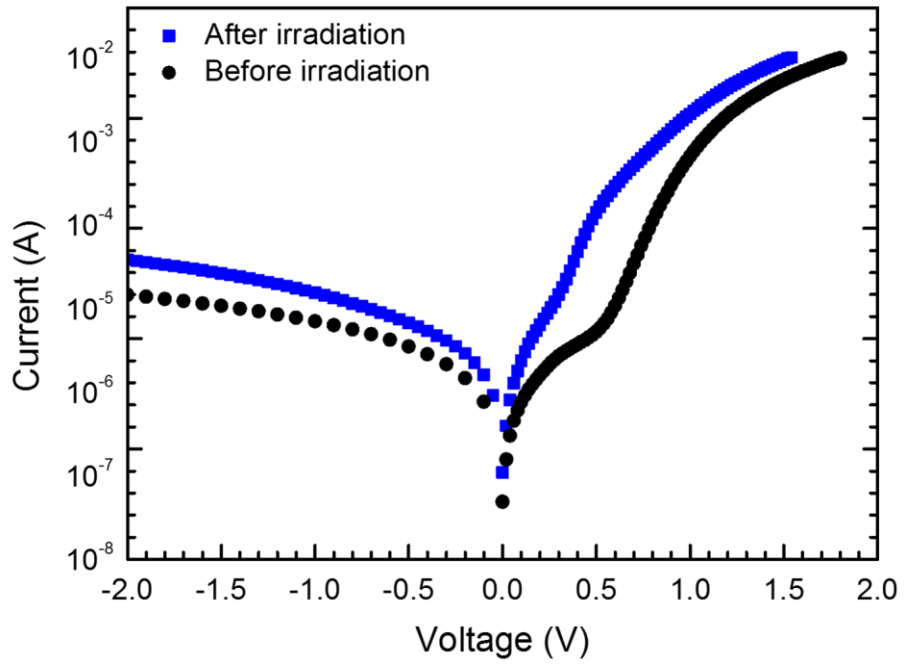


Figure 4.5: Room temperature semi-logarithmic plot of  $I$ - $V$  measurements of Pd/ZnO/n-Si/AuSb Schottky diode before and after irradiation with alpha-particles.

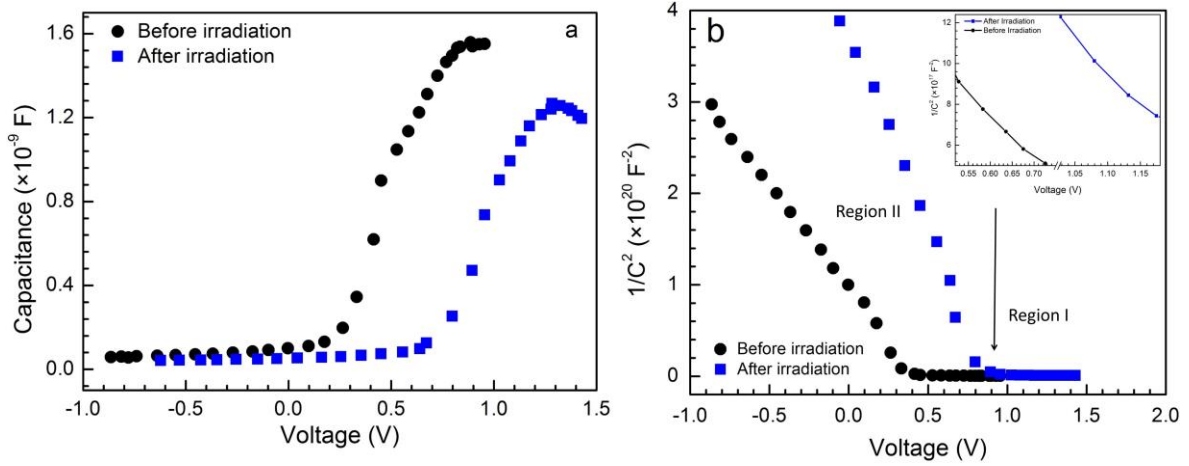


Figure 4.6:  $C$ - $V$  measurements before and after irradiation at room temperature at 1 MHz.

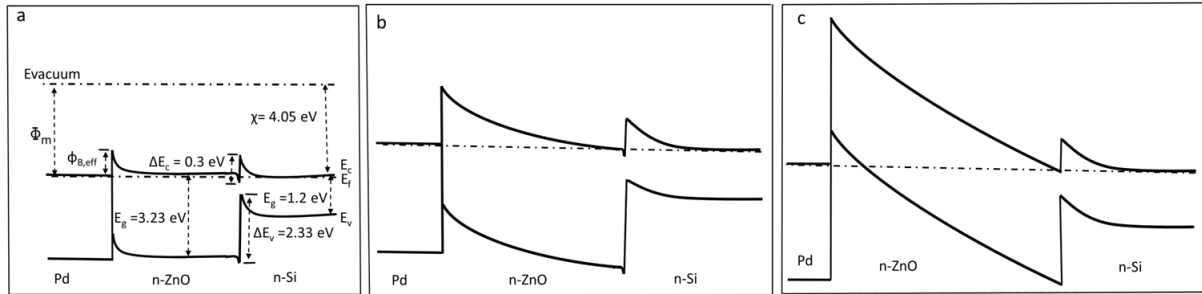


Figure 4.7: Energy band diagram of Pd/ZnO/n-Si heterojunction (a) Under thermal equilibrium (b) After applying a small reverse bias (c) After increasing the reverse bias.

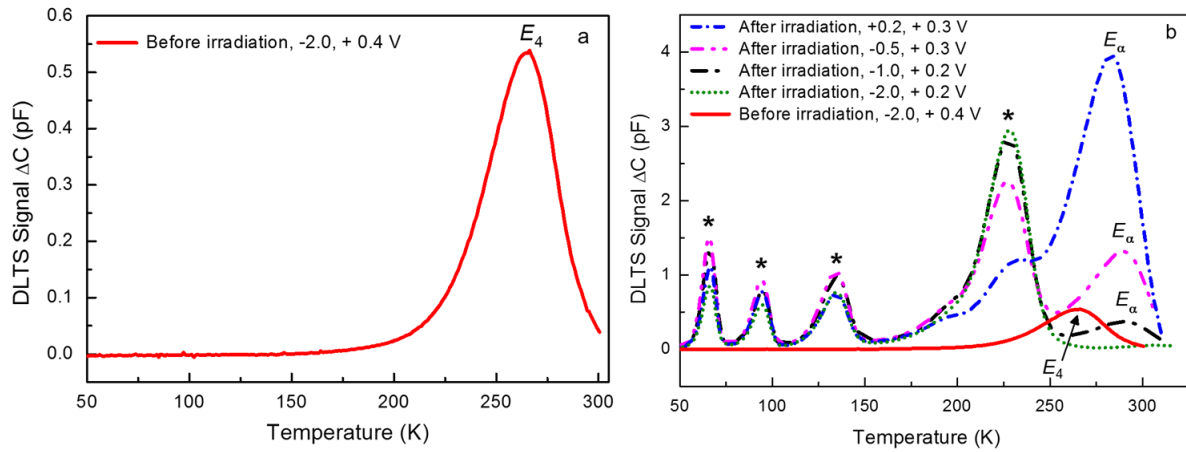


Figure 4.8: DLTS spectra obtained from Pd/ZnO/n-Si/AuSb Schottky diode (a) before and (b) after irradiation, recorded at different a quiescent reverse bias, different filling pulse amplitude, filling pulse width of 1 ms and rate window of 80.2 Hz in the temperature range 50 - 350 K.

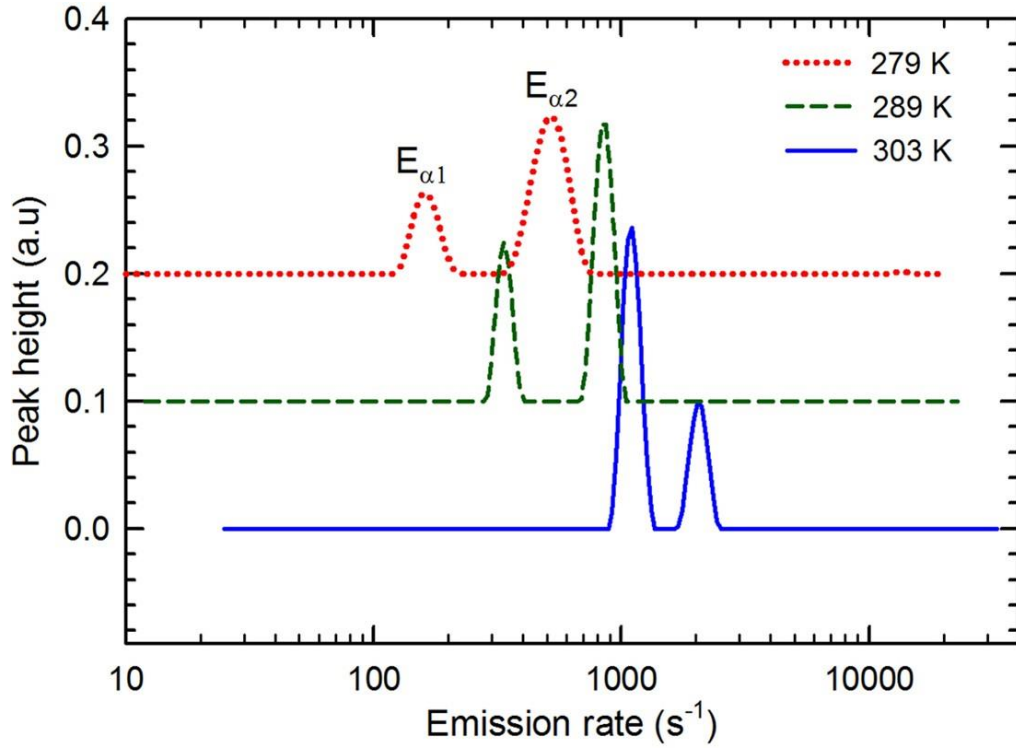


Figure 4.9: Laplace DLTS spectra showing the shift of  $E_{\alpha 1}$  and  $E_{\alpha 2}$  defects at three temperatures in ZnO thin films after irradiation.

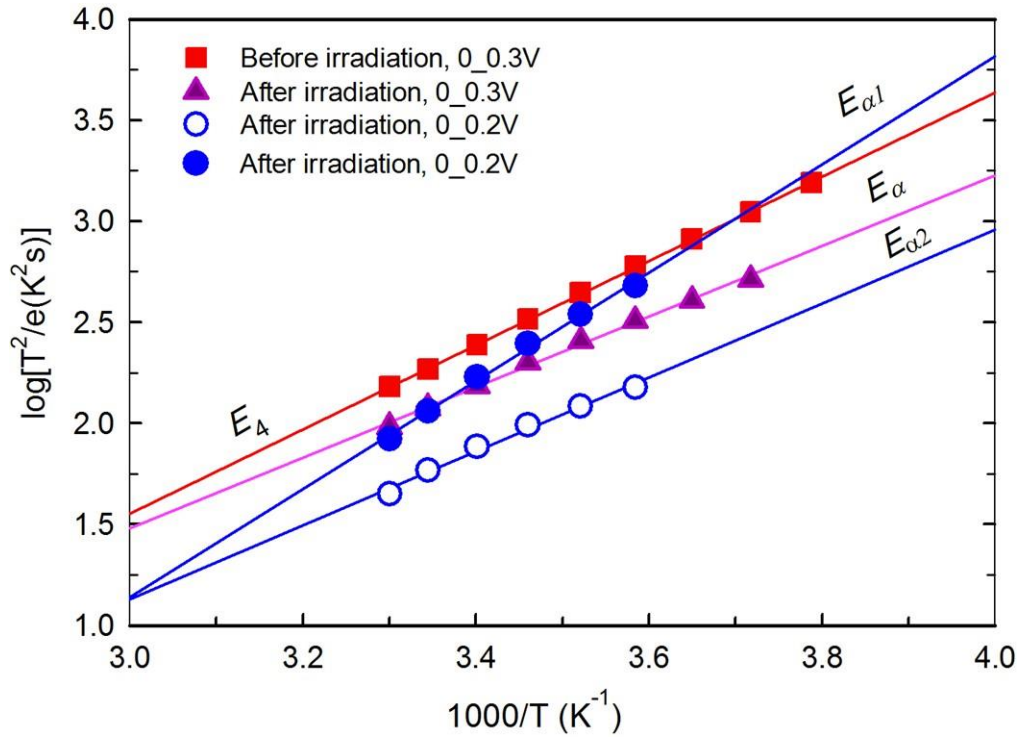


Figure 4.10: Arrhenius plots of the defects in ZnO thin films, obtained at a quiescent reverse bias of 0 V with a filling pulse amplitude of 0.3 V for  $E_4$ ,  $E_{\alpha}$  and 0.2 V for  $E_{\alpha 1}$  and  $E_{\alpha 2}$ . The filling pulse width was 1 ms.

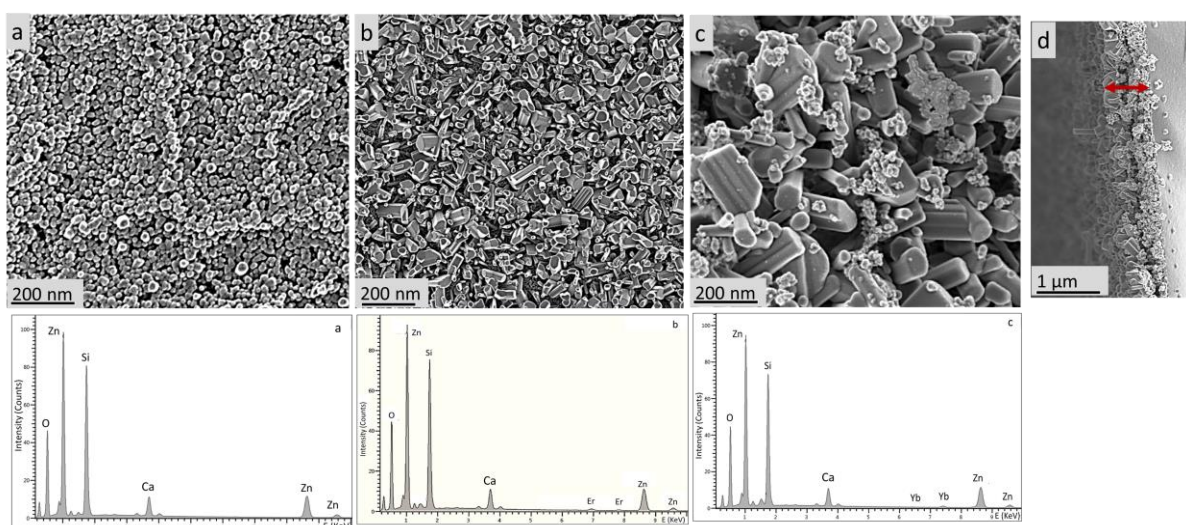


Figure 4.11: SEM images and EDS plot of (a) undoped ZnO (b) Er-doped ZnO (c) Yb-doped ZnO and (d) cross section of Yb-doped ZnO thin films deposited on microscope slide substrates, dried at 200 °C and annealed at 600 °C in air for 1 hour.

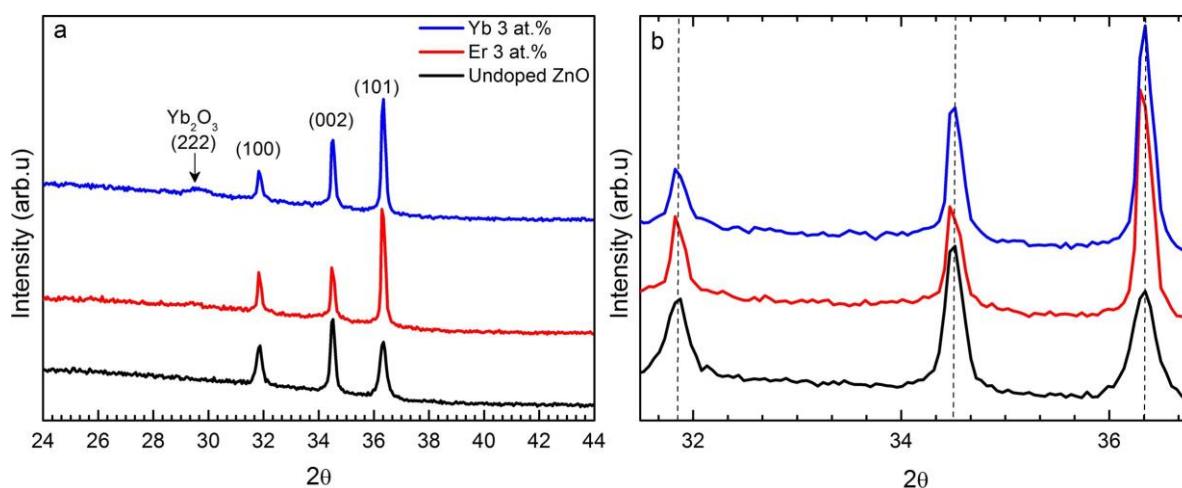


Figure 4.12: (Color online) (a) The X-ray diffraction (XRD) patterns of undoped, Er-doped and Yb-doped ZnO thin films deposited on microscope slide substrates, (b) enlargement showing the shift in the (100), (002) and (101) diffraction peaks of the doped films to lower angles compared to the undoped ZnO peak positions.



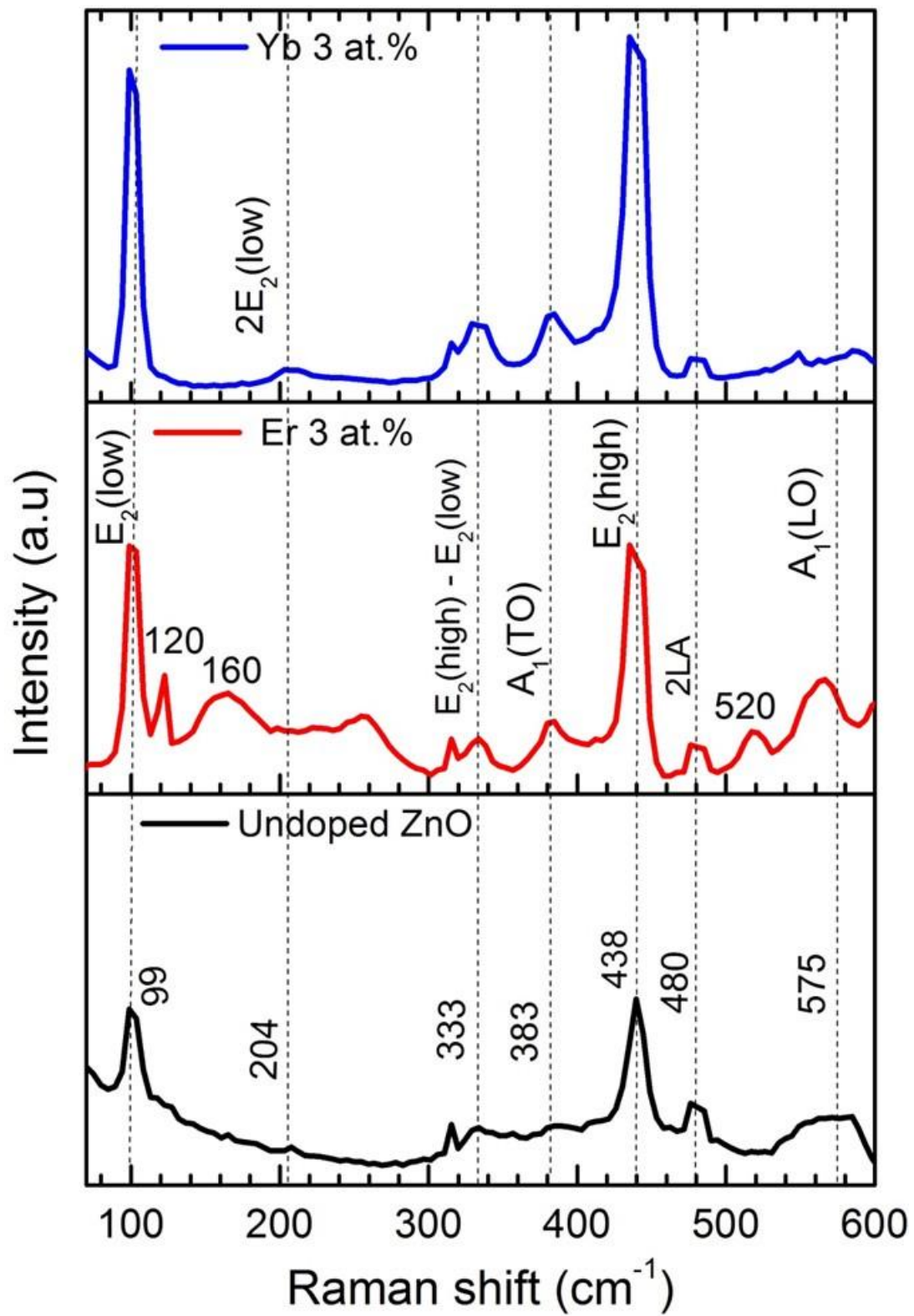


Figure 4.13: (Color online) Raman spectra of undoped, Er-doped and Yb-doped ZnO thin films deposited onto microscope slide substrates.



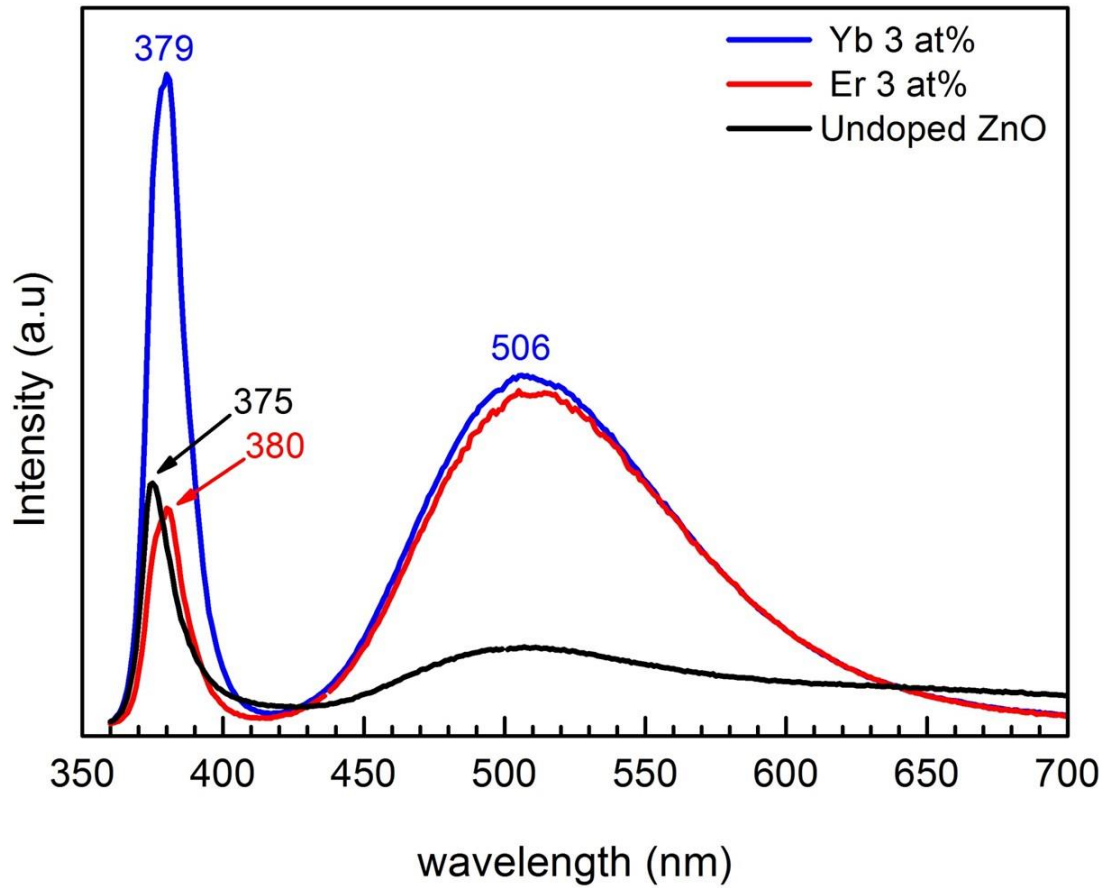


Figure 4.14: (Color online) The PL spectra of undoped, Er-doped and Yb-doped ZnO thin films deposited onto microscope slide substrates.

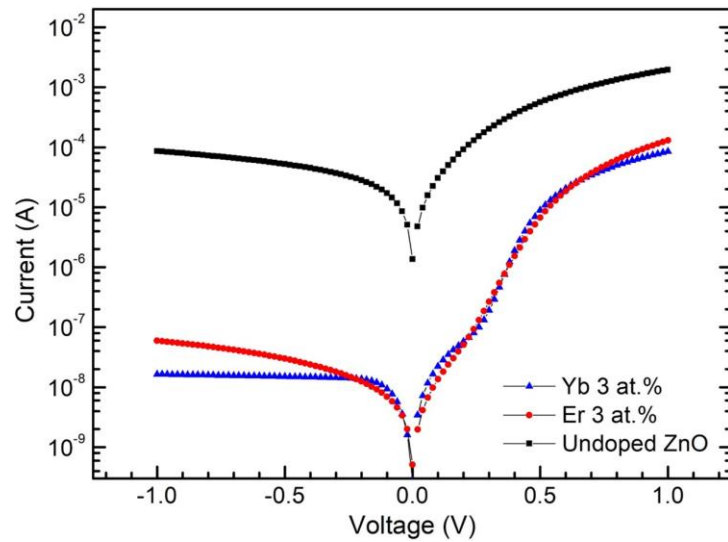


Figure 4.15: (Color online) Room temperature semi-logarithmic plot of  $I$ - $V$  measurements of Schottky diodes fabricated on undoped, Er-doped and Yb-doped ZnO thin films Schottky diodes.

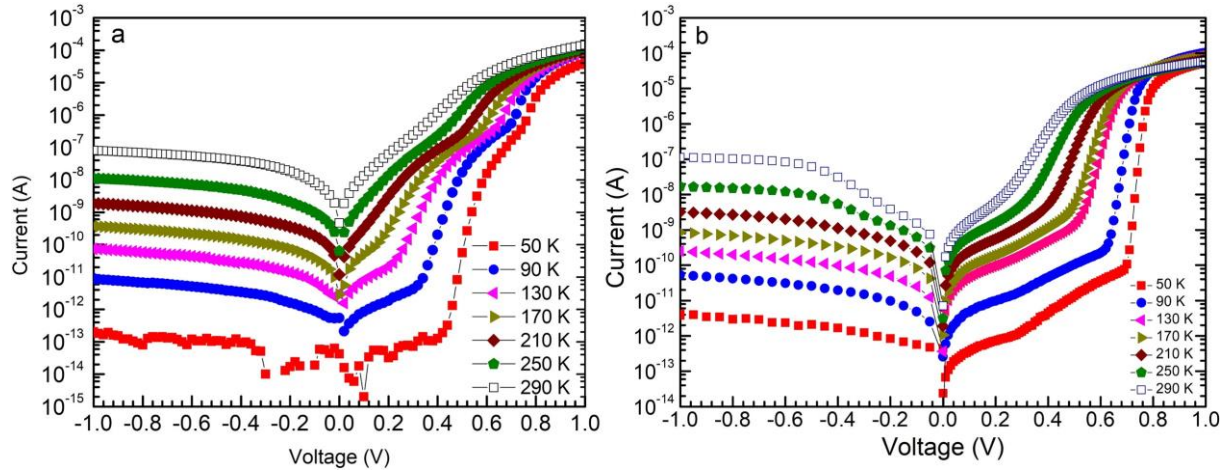


Figure 4.16: (Color online) Semi-logarithmic plot of  $I$ - $V$  measurements for (a) Pd/Er-doped ZnO/n-Si/AuSb (b) Pd/Yb-doped ZnO/n-Si/AuSb Schottky diodes in the temperature range of 50 - 290 K with steps of 40 K.

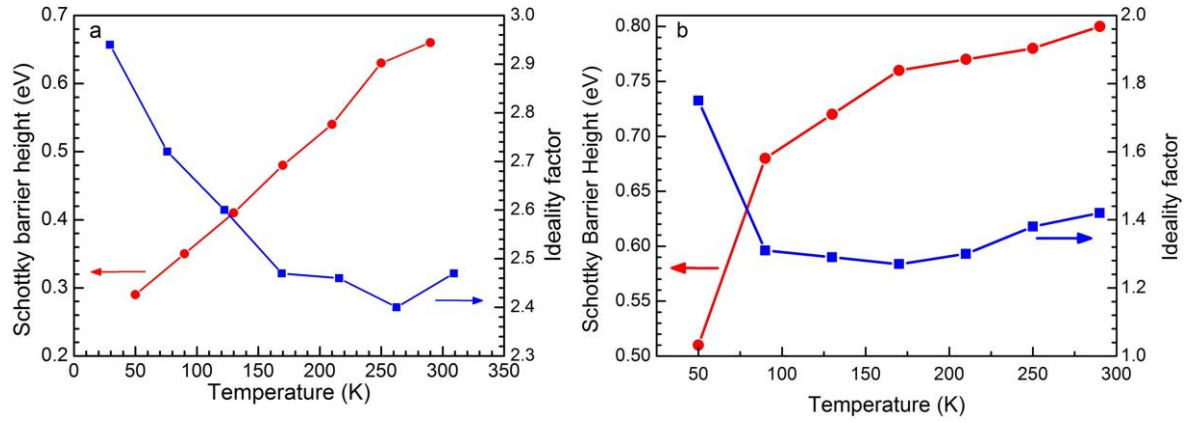


Figure 4.17: (Color online) SBH and ideality factor vs temperature plot from the forward bias  $I$ - $V$  measurements for (a) Pd/Er-doped ZnO/n-Si/AuSb (b) Pd/Yb-doped ZnO/n-Si/AuSb Schottky diodes in the temperature range of 50 - 290 K in steps of 40 K.

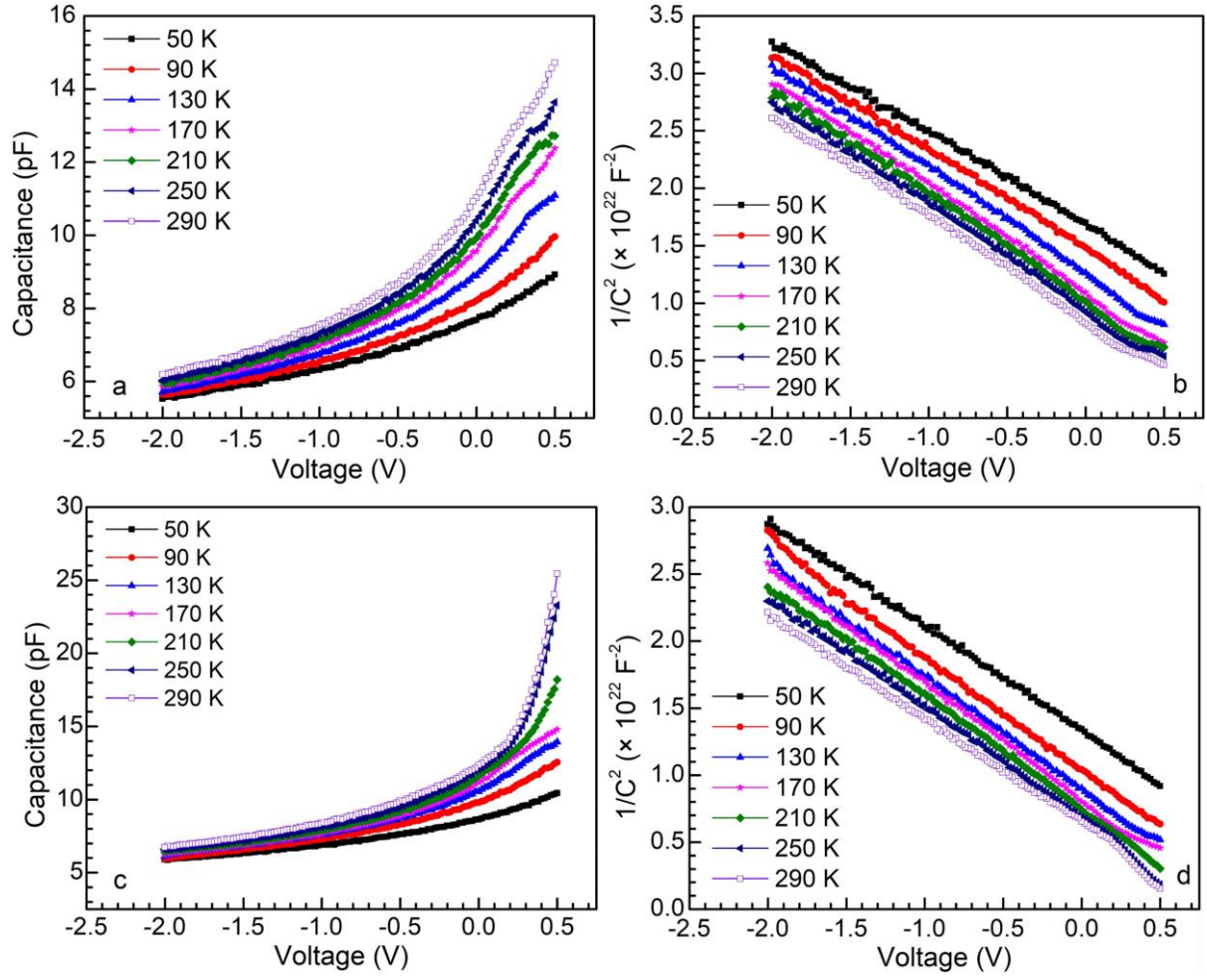


Figure 4.18: (Color online) C-V measurements of (a) and (b) Pd/Er-doped ZnO/n-Si/AuSb (c) and (d) Pd/Yb-doped ZnO/n-Si/AuSb Schottky diodes in the temperature range of 50 - 290 K at 1 MHz

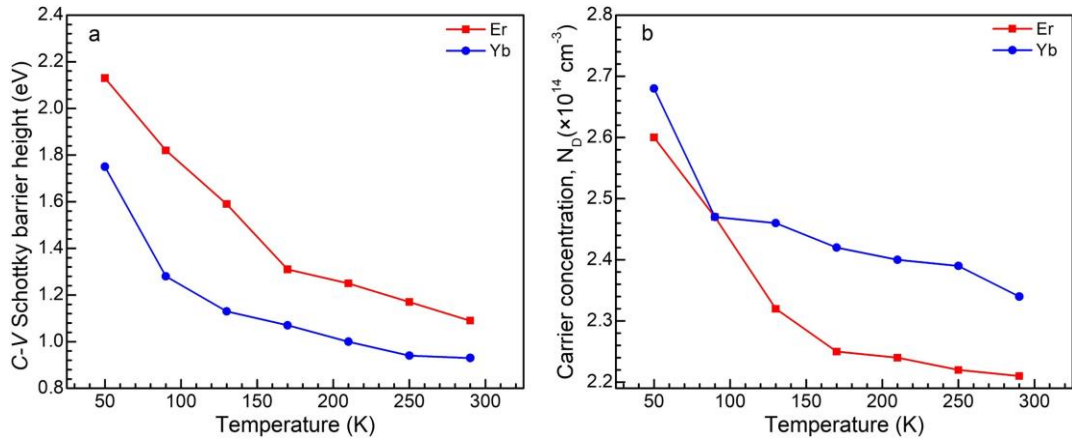


Figure 4.19: (Color online) SBH and carrier concentration vs temperature obtained from C-V measurements of (a) Pd/Er-doped ZnO/n-Si/AuSb (b) Pd/Yb-doped ZnO/n-Si/AuSb Schottky diodes in the temperature range of 50 - 290 K.

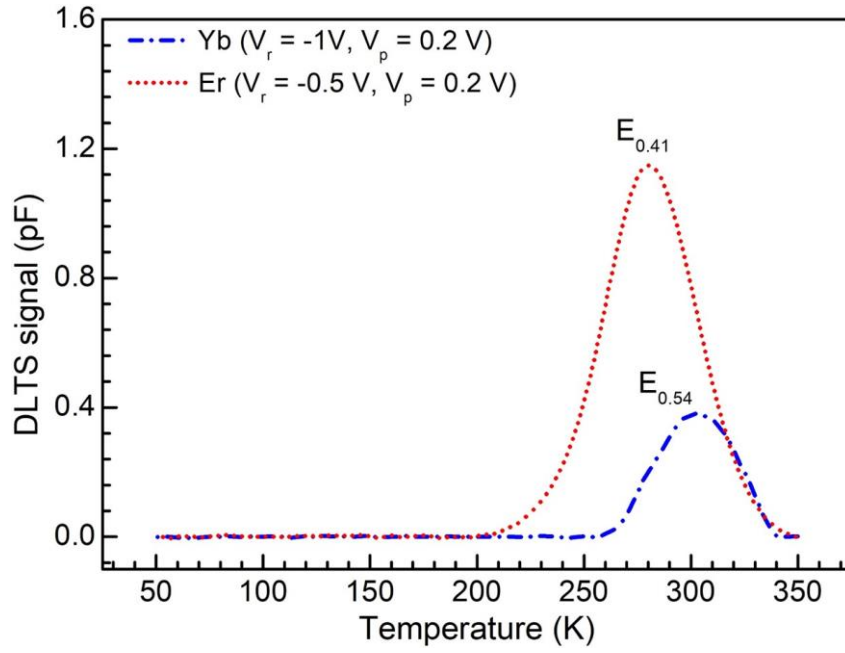


Figure 4.20: (Color online) DLTS spectra obtained from Pd/Er-doped ZnO/n-Si/AuSb and Pd/Yb-doped ZnO/n-Si/AuSb Schottky diodes, recorded at a quiescent reverse bias of  $V_r = -0.5$  and  $-1 V$  for the Er-doped and Yb-doped ZnO thin films, respectively. The filling pulse voltage  $V_p = 0.2 V$ , filling pulse width of 1 ms and rate window of 80 Hz in the temperature range of 50 - 350 K.

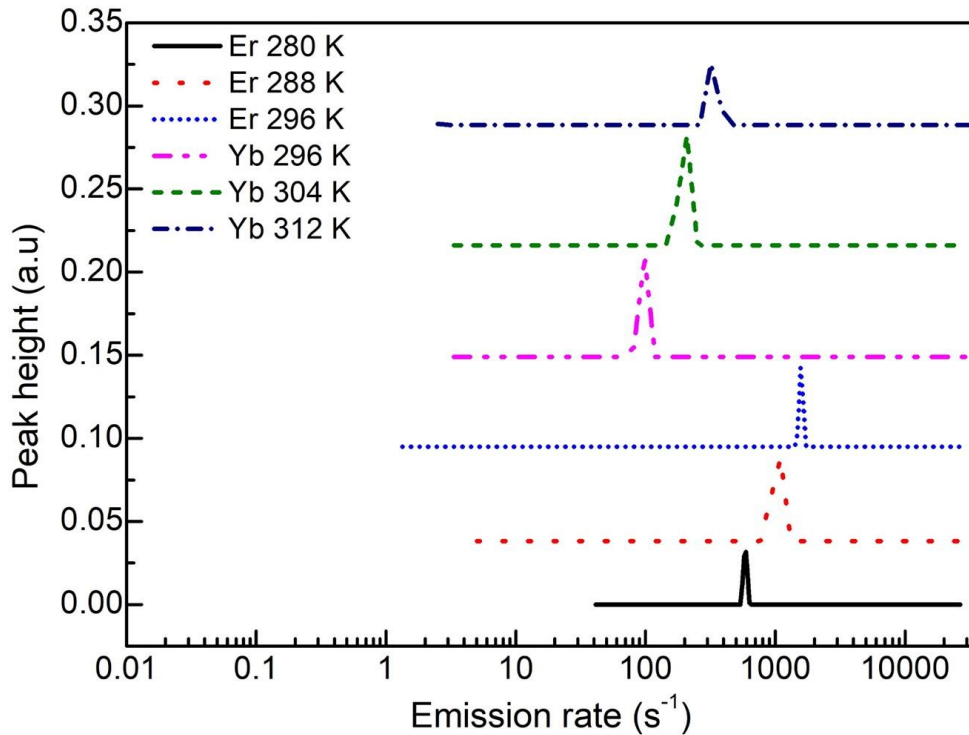


Figure 4.21: (Color online) Laplace DLTS spectra showing the shift of the defect in Er-doped and Yb-doped ZnO thin films at different temperatures.

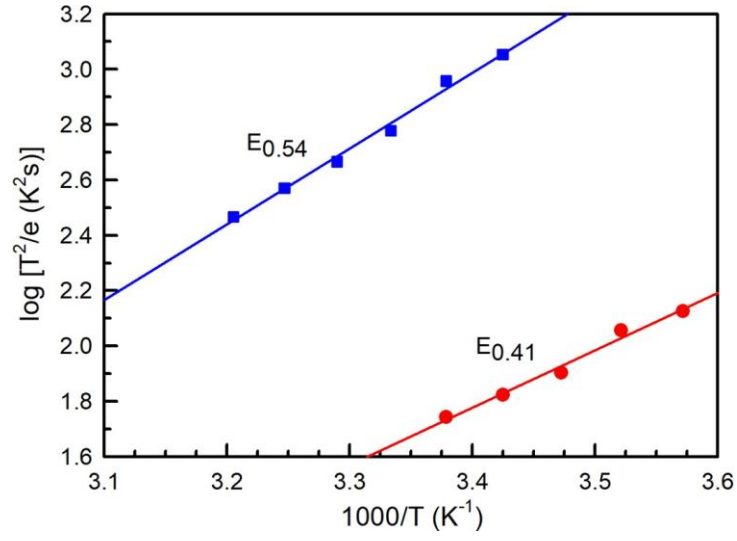


Figure 4.22: (Color online) Arrhenius plots of the defects in Er-doped and Yb-doped ZnO thin films.

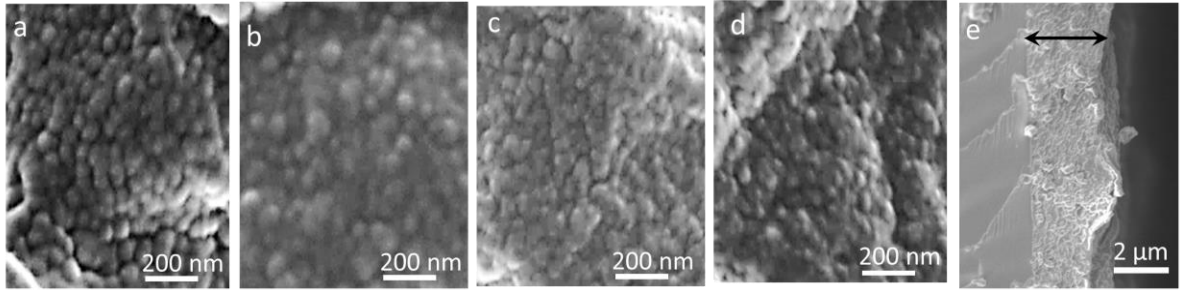


Figure 4.23: SEM images of ZnO thin films with (a) Er 0 at.% (b) Er 2 at.% (c) Er 4 at.% and (d) Er 6 at.% as well as (e) cross-section of Er 6 at.% deposited on microscope slides, dried at 200 °C and annealed at 500 °C in air for 1 hour.

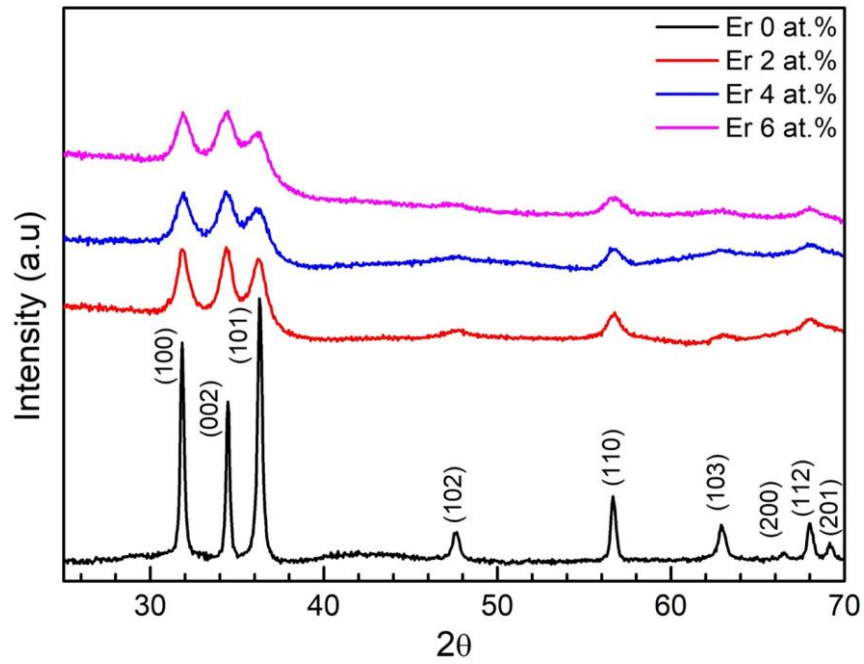


Figure 4.24: (Color online) X-ray diffraction (XRD) patterns of Er-doped ZnO thin films deposited onto microscope slides, dried at 200 °C and annealed at 500 °C in air for 1 hour.

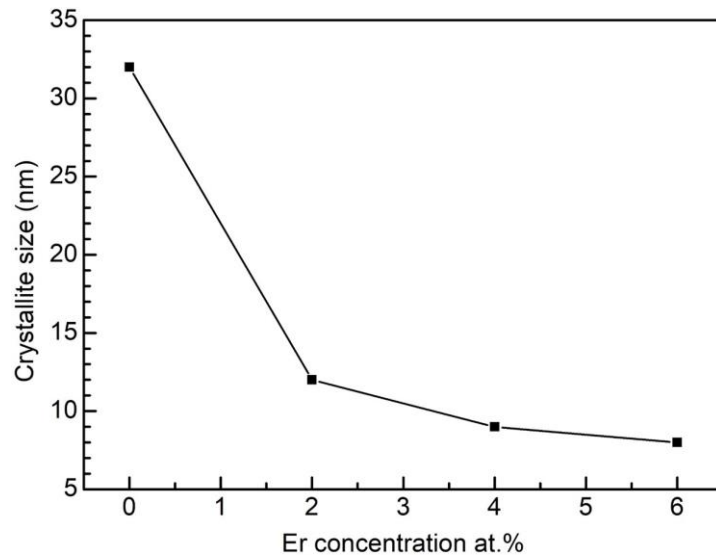


Figure 4.25: The crystallite size versus Er concentrations.



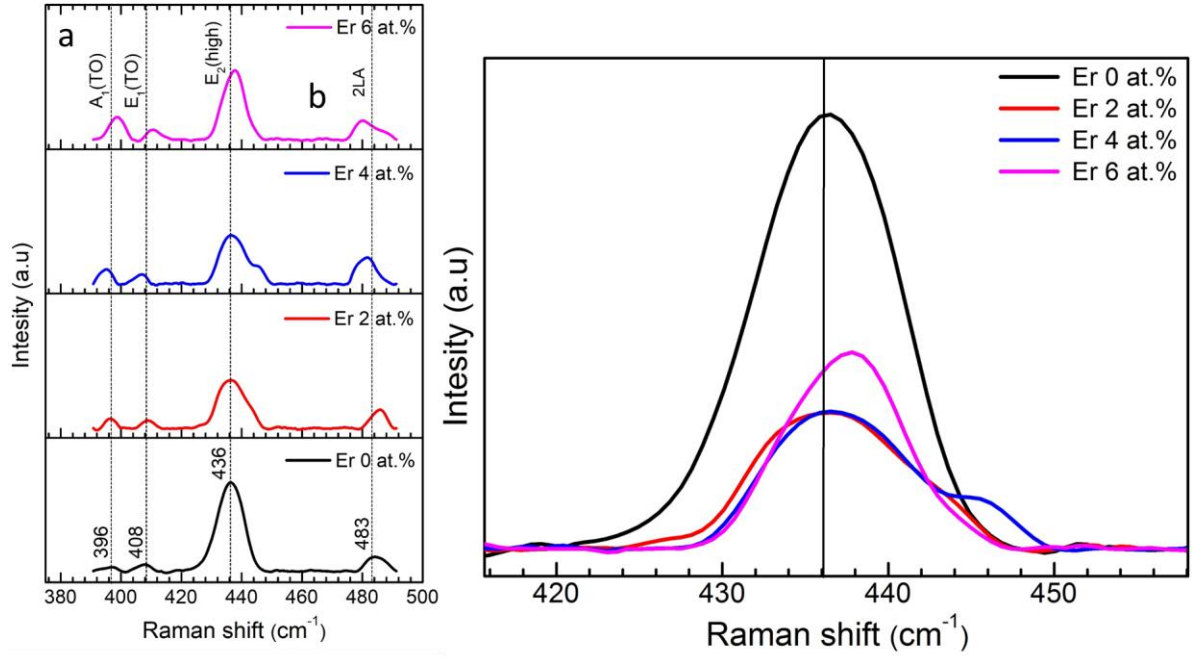


Figure 4.26: (Color online) (a) Raman spectra of the Er-doped ZnO thin films deposited onto microscope slides, dried at 200 °C and annealed at 500 °C in air for 1 hour (b) The shift of the  $E_2$  (high) mode.

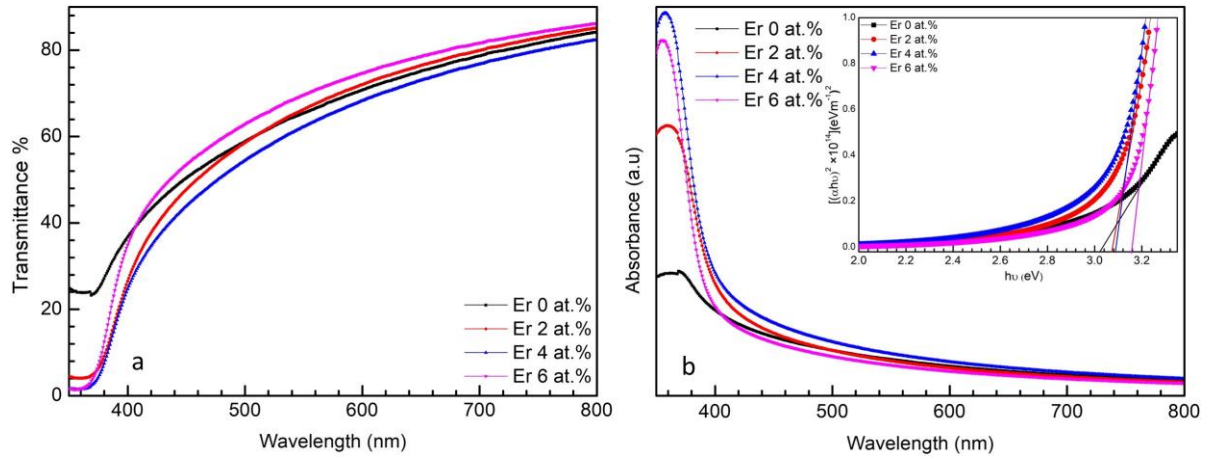


Figure 4.27: (Color online) UV-Vis spectra of (a) transmittance (b) absorbance and corresponding Tauc plot (inset) of the Er-doped ZnO thin films deposited on microscope slides, dried at 200 °C and annealed at 500 °C in air for 1 hour.

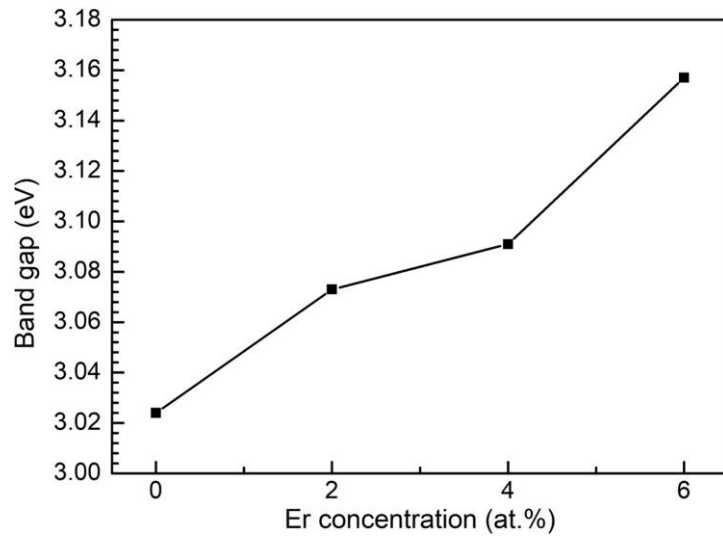


Figure 4.28: Band gap versus Er concentrations.

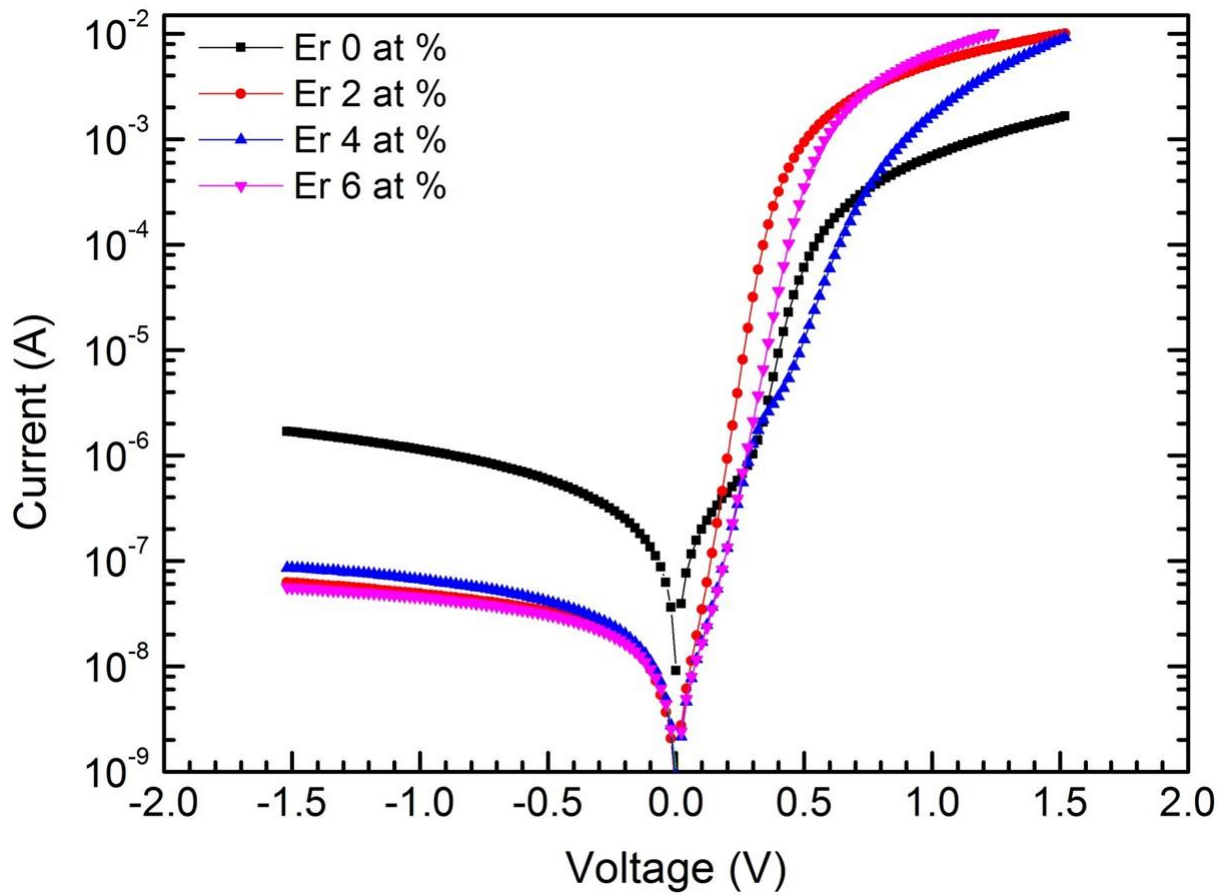


Figure 4.29: (Color online) Room temperature semi-logarithmic  $I$ - $V$  plot of Pd/Er-doped ZnO/n-Si/AuSb Schottky diodes.



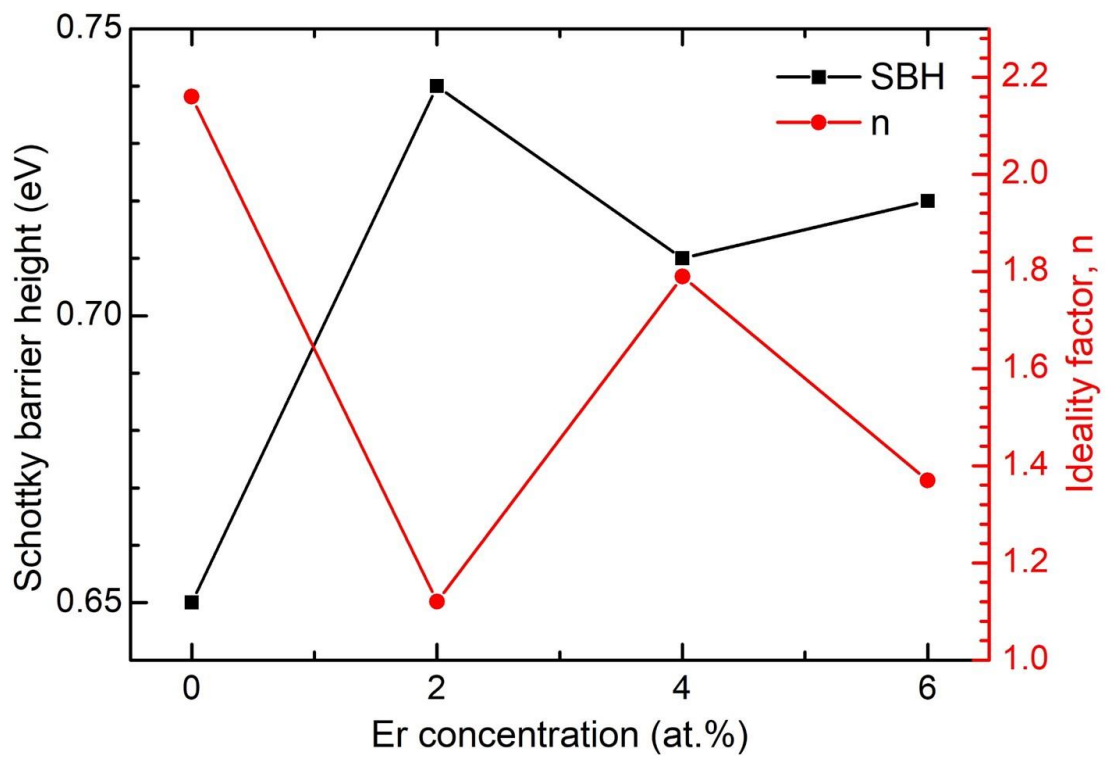


Figure 4.30: (Color online) SBH and ideality factor vs the Er concentration plot from the forward bias  $I$ - $V$  measurements for Pd/Er-doped ZnO/n-Si/AuSb Schottky diodes.

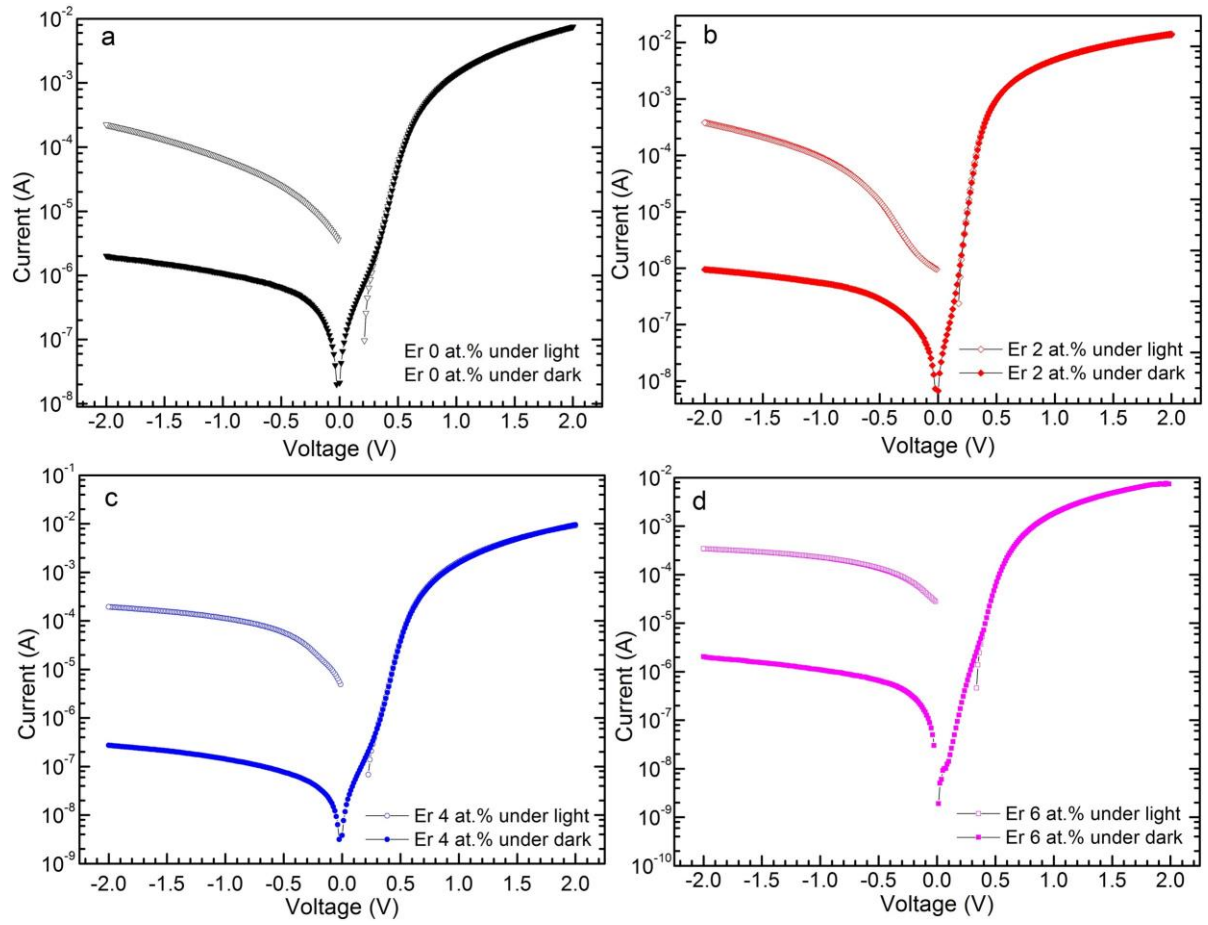


Figure 4.31: (Color online) Room temperature semi-logarithm  $I$ - $V$  measurements under dark and illumination of Pd/Er-doped ZnO/n-Si/AuSb Schottky diodes.

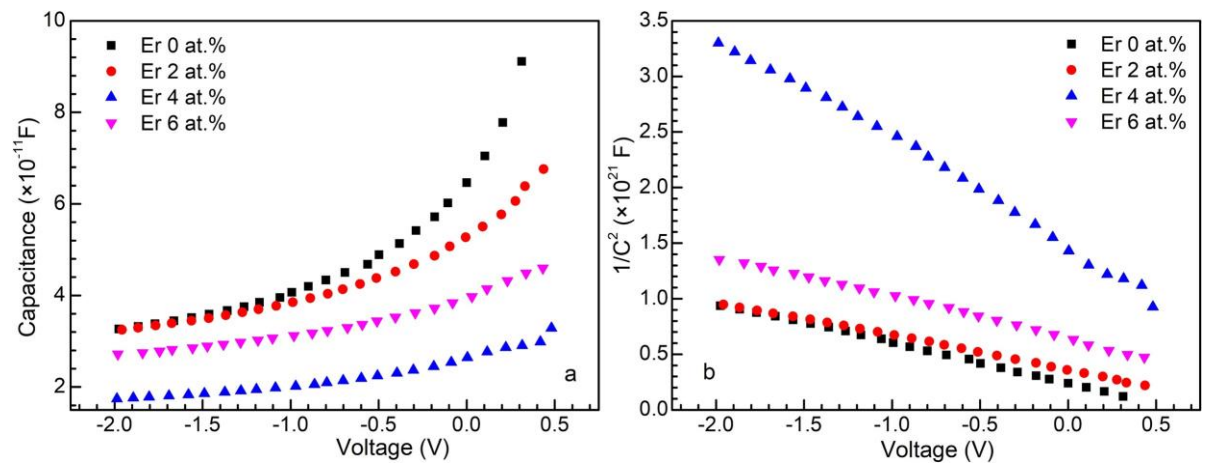


Figure 4.32: (Color online) Room temperature  $C$ - $V$  measurements of Pd/Er-doped ZnO/n-Si/AuSb Schottky diodes at 1 MHz.

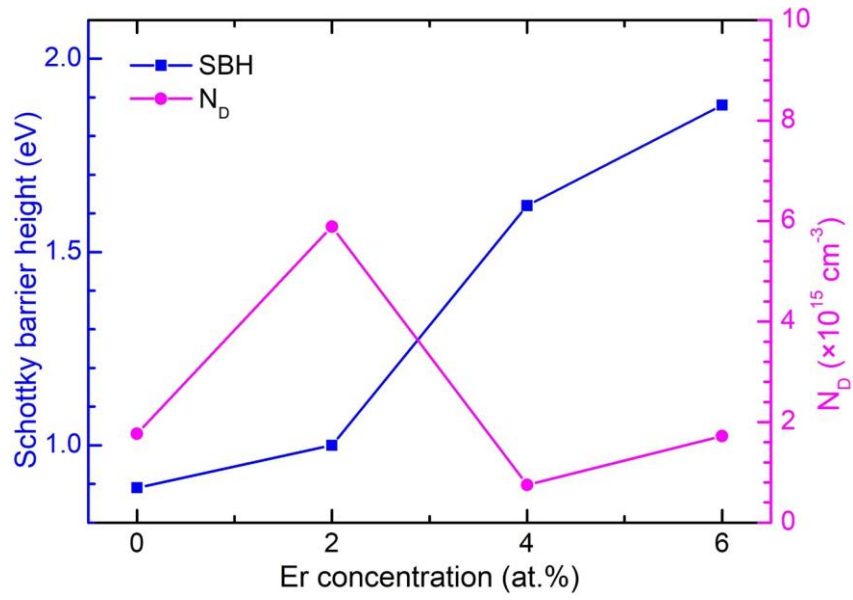


Figure 4.33: (Color online) SBH and carrier concentration vs the Er concentration obtained from  $C$ - $V$  measurements of Pd/Er-doped ZnO/n-Si/AuSb Schottky diodes.

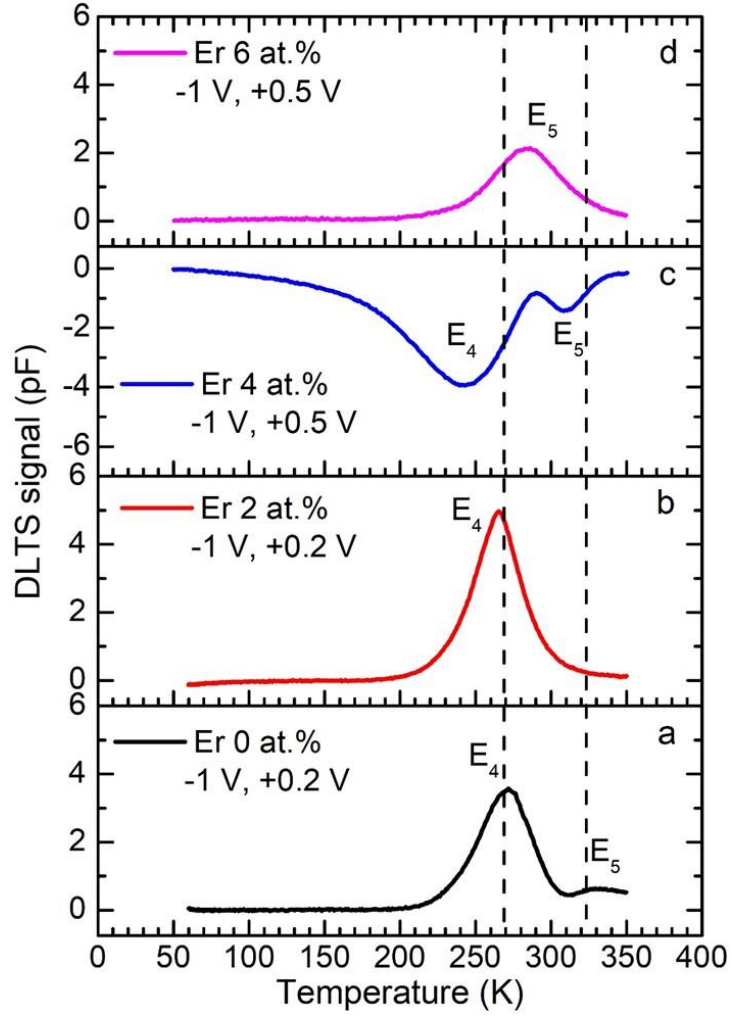


Figure 4.34: (Color online) DLTS spectra obtained from Pd/Er-doped ZnO/n-Si/AuSb Schottky diodes, recorded at a quiescent reverse bias  $V_r = -1$  V, filling pulse voltage  $V_p = 0.2$  V for Er 0 and 2 at.%, and 0.5 V for Er 4 and 6 at.%, filling pulse width of 1 ms and rate window of 80 Hz in the temperature range of 50 - 350 K.

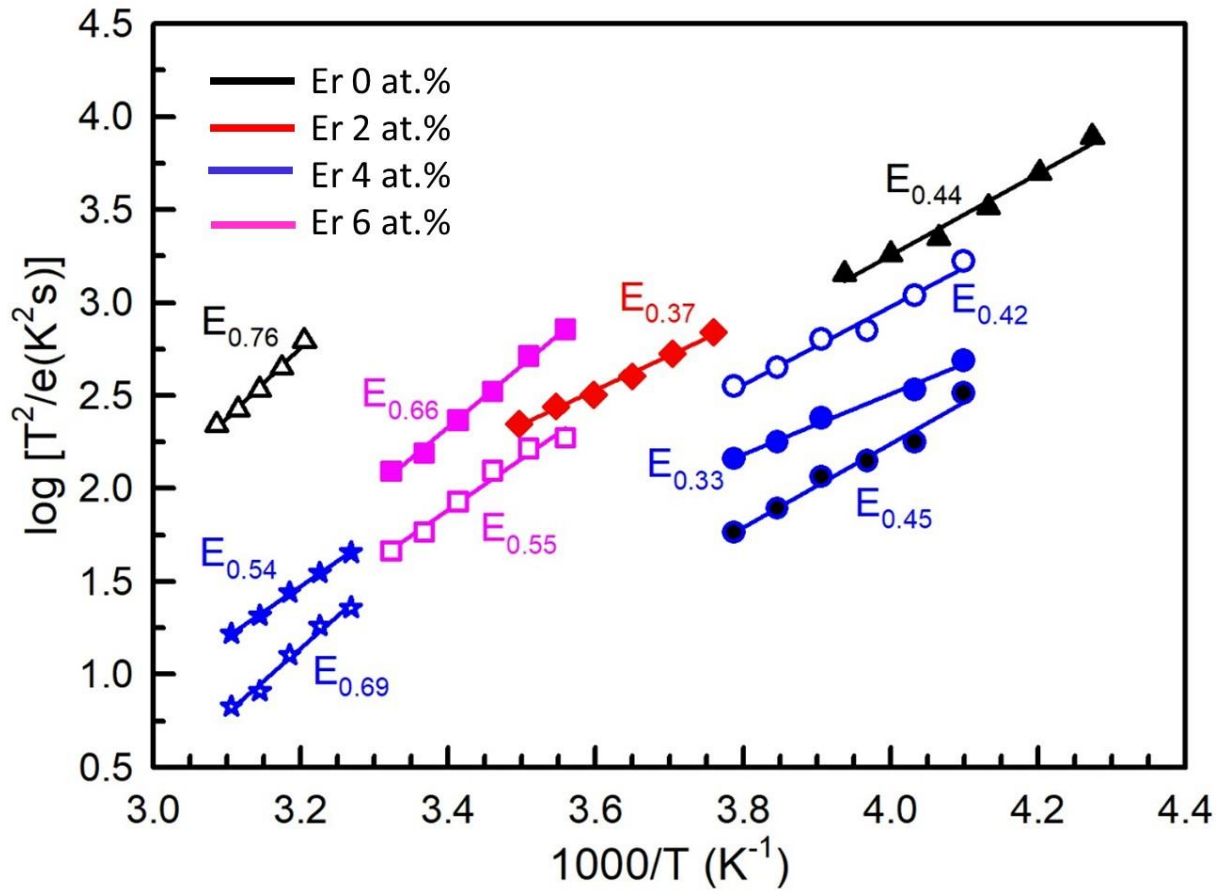


Figure 4.35: (Color online) Arrhenius plots of the defects in Pd/Er-doped ZnO/n-Si/AuSb Schottky diodes.

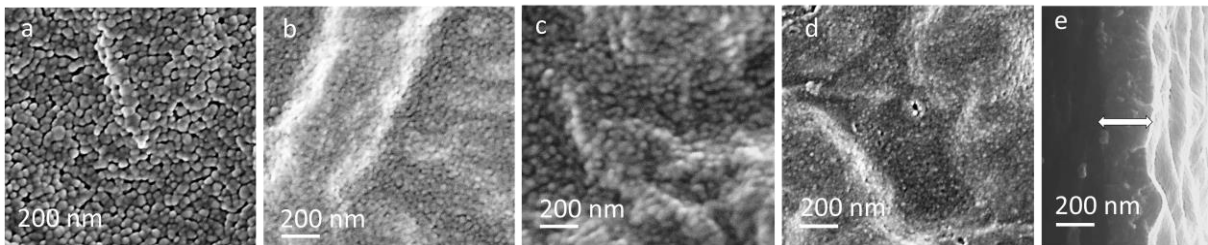


Figure 4.36: SEM images of (a) 0 at.% (b) 2 at.% (c) 4 at.% and (d) 6 at.% as well as (e) cross section of (Er, Yb) co-doped 6 at.% deposited on microscope slides, dried at 200 °C and annealed at 500 °C in air for 1 hour.

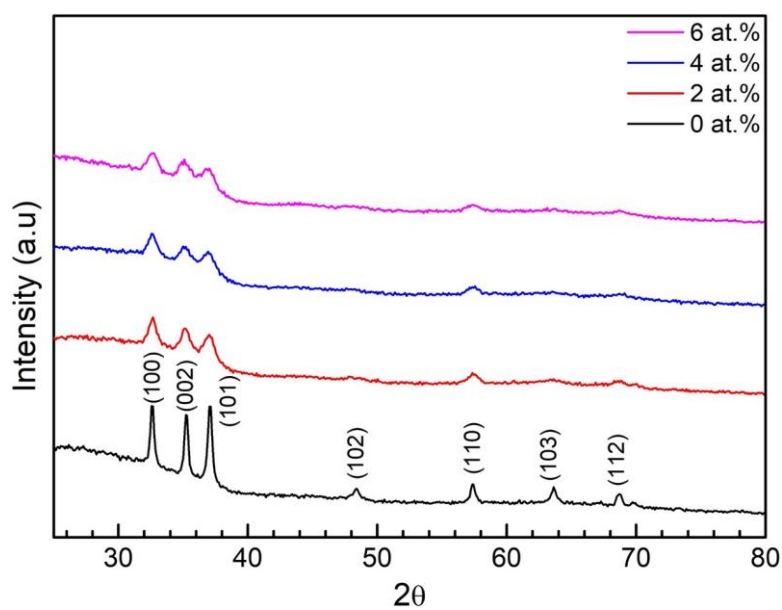


Figure 4.37: (Color online) The X-ray diffraction (XRD) patterns of Er and Yb co-doped ZnO thin films deposited onto microscope slides, dried at 200 °C and annealed at 500 °C in air for 1 hour.

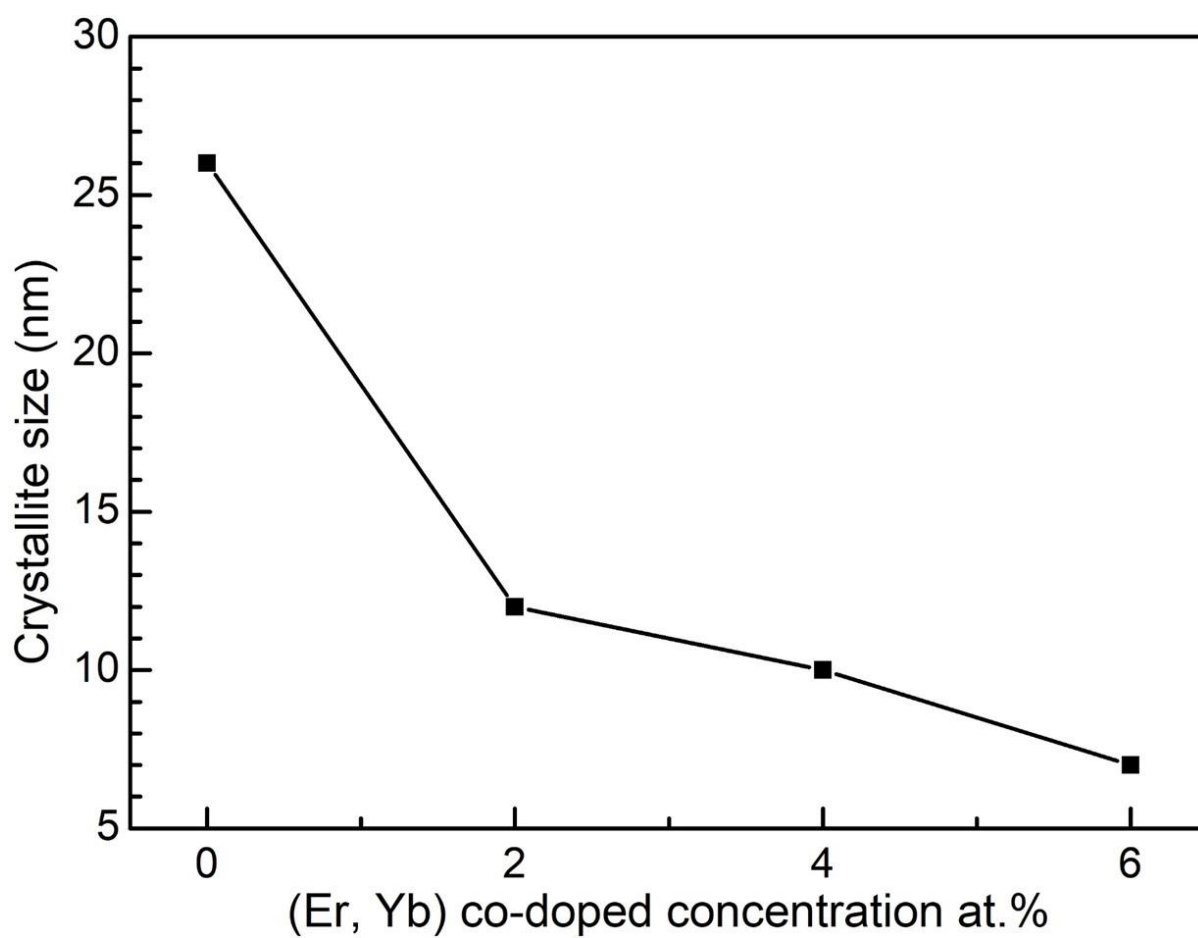


Figure 4.38: The crystallite size versus (Er, Yb) concentrations.

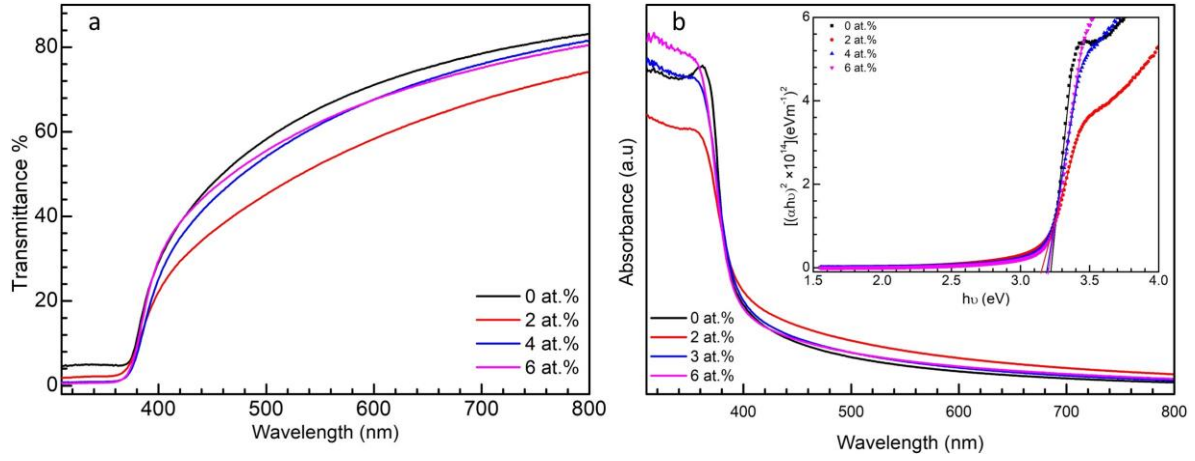


Figure 4.39: (Color online) UV-Vis spectra of (a) transmittance (b) absorbance and corresponding Tauc plot (inset) of (Er, Yb) co-doped ZnO thin films deposited on microscope slides, dried at 200 °C and annealed at 500 °C in air for 1 hour.

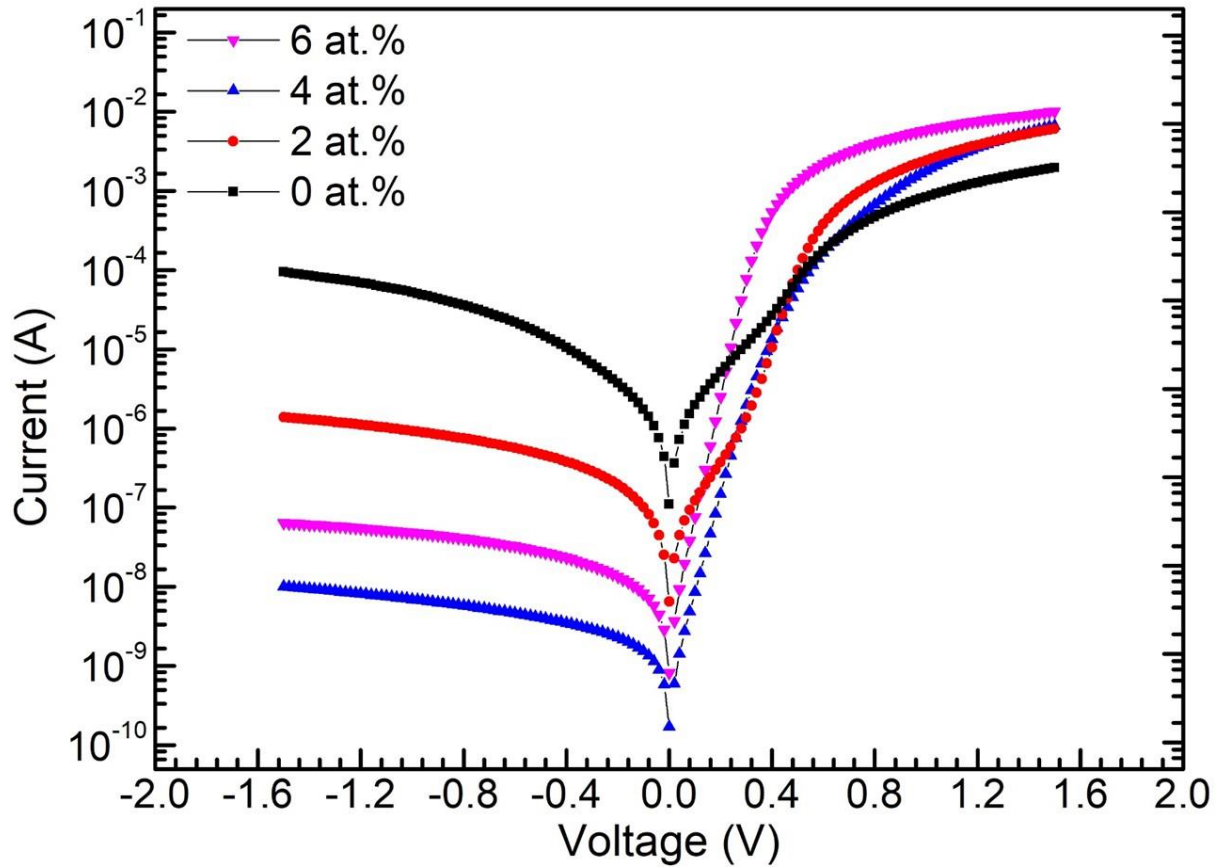


Figure 4.40: Color online) Room temperature semi-logarithmic plot of  $I$ - $V$  measurements of Pd/(Er, Yb) co-doped ZnO/n-Si/AuSb Schottky diodes.



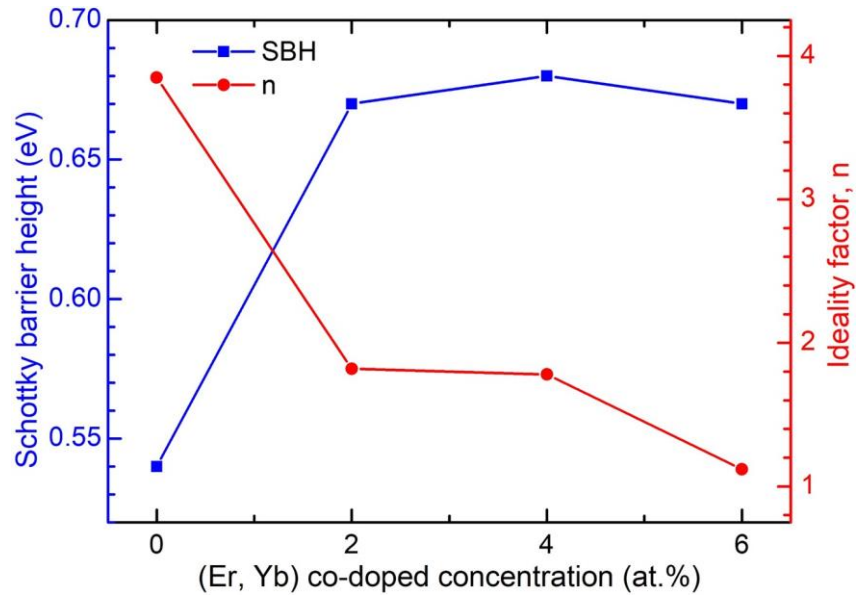


Figure 4.41: Color online) SBH and ideality factor vs (Er, Yb) co-doped concentration plot from the forward bias  $I$ - $V$  measurements for Pd/(Er, Yb) co-doped ZnO/n-Si/AuSb Schottky diodes.

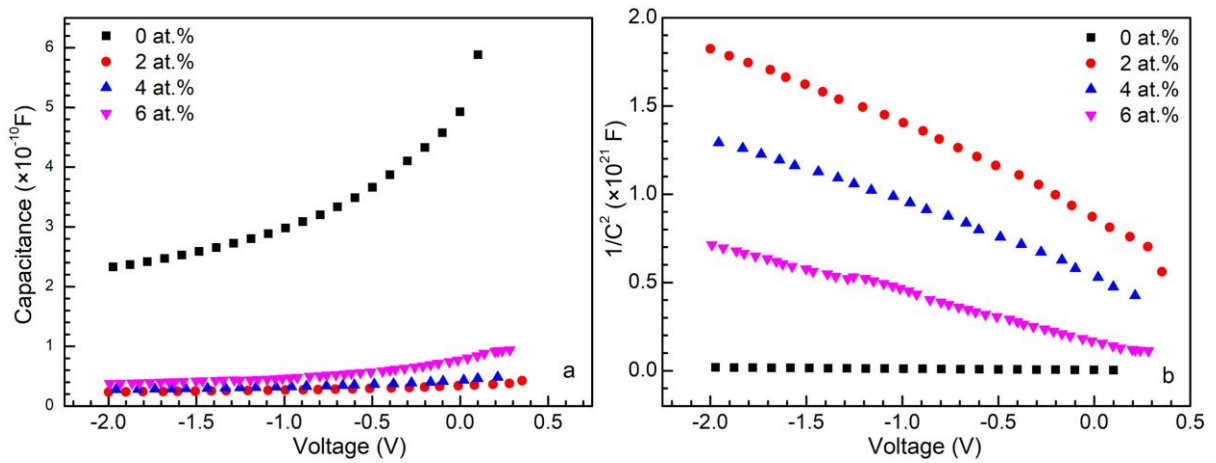


Figure 4.42: (Color online) Room temperature  $C$ - $V$  measurements of Pd/(Er, Yb) co-doped ZnO/n-Si/AuSb Schottky diodes measured at 1 MHz.



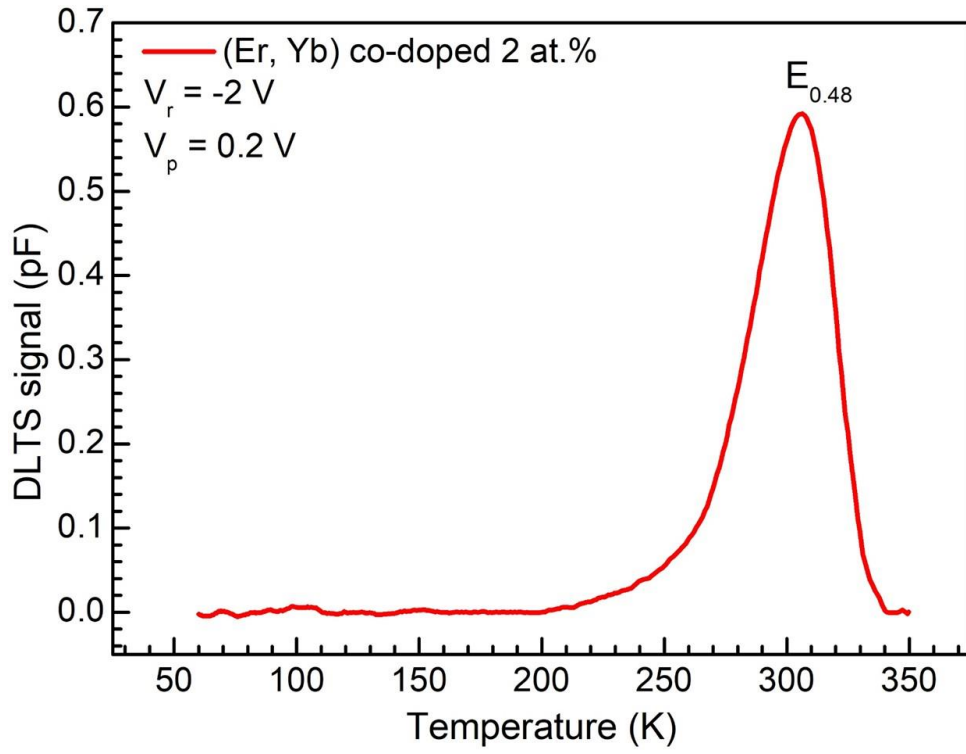


Figure 4.43: DLTS spectra obtained from Pd/(Er, Yb) co-doped ZnO/n-Si/AuSb Schottky diodes, recorded at a quiescent reverse bias  $V_r = -2$  V, filling pulse voltage  $V_p = 0.2$  V, filling pulse width of 1 ms and rate window of 80 Hz in the temperature range of 50 - 350 K.

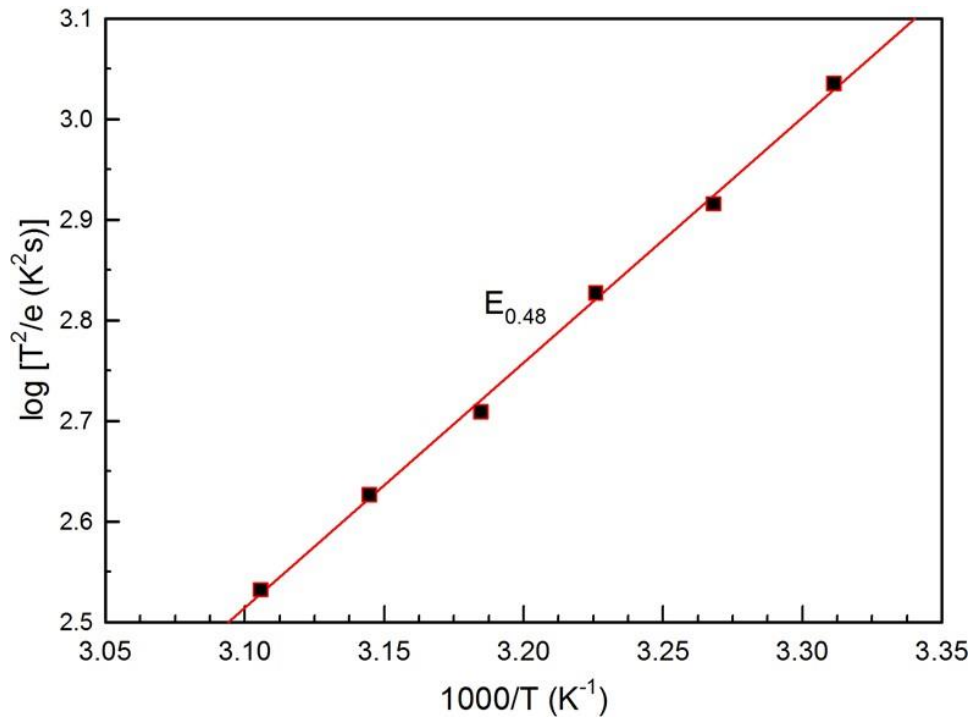


Figure 4.44: Arrhenius plots of the defect in (Er, Yb) 2 at.% co-doped ZnO thin films